Satellite Planes in Alternative Dark Matter (ADM) Models

Soumya Dhavale

Matrikel-Nr. 825579

A Master's Thesis submitted for evaluation for

Master of Science, Astrophysics

Faculty of Mathematics and Natural Sciences

University of Potsdam

Supervisor: Dr. Marcel S. Pawlowski (AIP)
Second Supervisor: Prof. Dr. Maria-Rosa Cioni (University of Potsdam, AIP)

Date of declaration: 28. January, 2026
Date of submission: 13. July, 2026

Abstract

Our current picture of cosmology is incomplete without accounting for some form of invisible matter in the makeup of our Universe. We name this invisible matter *dark matter*, and it makes up around a quarter of the Universe's matter content. Dark matter solves several problems in astrophysics and cosmology, ranging from the rotation curves of galaxies to the large-scale structure of the Universe.

The exact nature of dark matter is under debate and an active area of research. We assume an inert type of particle dark matter, termed Cold Dark Matter (CDM), and this governs our current understanding of cosmology. However, in the late twentieth century, several unanswered questions began to emerge and challenge this assumption. Especially on the smaller scales, where simulations and observations could not agree, there appears to be a need for modifications to the current paradigm. One such active area of research is the planes of satellite galaxies problem, which remains debated in terms of its causes and the low likelihood of appearance in simulations.

In this work, I explore the possibility that alternative dark matter models — ADM, for short — may provide another avenue for research. Using simulation data from AIDA-TNG, where the authors simulate ADM models on a cosmological level, I fit planes to the ten most luminous satellites of Milky Way-like hosts in the CDM, velocity-dependent Self-Interacting Dark Matter (vSIDM), and Warm Dark Matter of particle mass 3 keV (WDM3) models of the simulation using the tensor of inertia (TOI). The kinematic coherence of the planes is also assessed. To the research question of whether more satellite planes can be produced by altering the underlying dark matter model, I report no significant effect. On the kinematics aspect of planar motion, there is also no significant effect. There is some deviation from the isotropic case, however: dark matter models favor flatter distributions and greater kinematic coherence than their isotropic counterparts.

Zusammenfassung

Dunkle Materie ist ein relevantes kosmologisches Phänomen, da es ein Viertel der Masse des Universums ausmacht und damit fünfmal soviel Dunkle Materie vorhanden ist als baryonische Materie. Durch das ΛCDM Kosmologie Modell wird Dunkle Materie als kalt und ohne Eigenwechselwirkung definiert. Es lagert sich in Potenzialtöpfen und Filamenten an, um das kosmische Netz zu bilden, wobei es die Entwicklung der baryonischen Materie beeinflusst, um Galaxien und Galaxienhaufen zu bilden. Diese Entwicklung entspricht dem Konzept der hierarchischen Strukturbildung, wobei es Homogenität und Isotropie gehorcht, was die Grundsteine der Kosmologie sind.

Der Erfolg der Dunklen Materie, auch CDM genannt, ist auf großen Skalen offensichtlich. Beweise dafür sind Beobachtungen der großen Strukturen mithilfe von mehreren Messungen und die Reproduzierbarkeit von dem kosmischen Mikrowellenhintergrund (CMB) in Simulationen basierend auf Lambda CDM. Simulationen bestärken die Prognosen dieser Theorie was Galaxien und Strukturentwicklung angeht, was den Vorteil hat, dass diese eine lange Zeitspanne abdecken, die es sonst nicht möglich ist zu beobachten. Auf kleinen Skalen gibt es aber Probleme.

Mehrere Fragen kommen durch die ΛCDM Theorie auf. Die wichtigsten davon für die vorliegende Arbeit sind die, die sich mit Dunkler Materie beschäftigen. Diese Probleme sind z.B. das Problem der fehlenden Satelliten, das Too-Big-To-Fail Problem, das Cusp-Core Problem und das hier relevanteste: das Problem der Satellitenebenen. Manche dieser Probleme können dadurch gelöst werden, dass man baryonische Physik mit der Physik der Dunklen Materie kombiniert. Andere benötigen noch Erklärungen, da baryonische Physik alleine nicht genügt. Solch ein Problem ist das der Satellitenebenen.

Es wurde in mehreren Galaxien beobachtet, dass deren Satelliten - Zwerggalaxien - die Galaxie (z.B. die Milchstraße oder Andromeda) bevorzugt in abgeflachten Verteilungen umkreisen. Wenn man Galaxien mit ihren Satelliten analog zu realen Systemen in Lambda CDM simuliert, ist diese Anordnung außerordentlich selten. Drei bis vier solcher Systeme in Beobachtungen zu finden, obwohl selbst ein System sehr selten ist, wirft die Frage auf, warum sich solche Systeme bilden. In allen vorgeschlagenen Erklärungen gibt es kein einziges Phänomen, das die Frage vollkommen beantwortet. Bisher unerforschte Möglichkeiten sind alternative Dunkle Materie (ADM) Modelle.

Der hier vorliegende Text ist eine Masterarbeit über das Vorkommen von Satellitenebenen in ADM-Modellen. Die Arbeit basiert auf den vor kurzem veröffentlichten AIDA-TNG Simulationen. Diese Simulationen basieren auf der bekannten Illustris-TNG Simulation, die aus drei kosmologischen Simulationen, die sich in der ΛCDM Kosmologie entwickeln, besteht. AIDA-TNG fügt zusätzlich zu den bestehenden CDM Modellen noch ADM Modelle hinzu. Die Modelle, die in der vollständigen Datenveröffentlichung beurteilt worden, sind warme Dunkle Materie mit Teilchenmassen (1, 3, 5) keV (WDM1, WDM2, WDM3), kalte Dunkle Materie (CDM) und selbstinteragierende Dunkle Materie (SIDM) mit konstantem Querschnitt (SIDM1) oder einem geschwindigkeitsabhängendem Querschnitt (vSIDM).

Die vorliegende Arbeit schaut auf drei Modelle: CDM, WDM3, vSIDM in jeweils einer 51,7 Mpc großen Simulationsbox. Diese Boxen bieten bessere Auflösungen als 100 Mpc große Boxen. Die Datensets wurden nach Milchstraßenanalogen bezüglich ihrer Virialmasse und der darin liegenden Satelliten, die Sternenmasse und mehr als 80% Dunkle Materie haben, gefiltert. Die zehn leuchtstärksten Satelliten jeder solchen Galaxie wurden zuerst nach ihrer räumlichen Anordnung und dann nach ihrer kinematischen Kohärenz beurteilt. Die Systeme wurden ebenfalls in einer komplett isotropischen Umgebung beurteilt.

Auf Basis der räumlichen Anordnung wurde ein Trägheitstensor (TOI) - Ebenen - Fitting Algorithmus benutzt, um die Normale für den besten Ebenenfit zu erfassen, das Achsenverhältnis, um das relative Abflachen zu messen, die RMS Höhe, um das absolute Abflachen jeder Ebene zu messen, und die RMS radiale Ausdehnung, um etwas über die radiale Verteilung zu lernen. Diese Größen wurde mit ihren isotropischen Gegenstücken verglichen. Die Modelle vergleichen

ebenfalls den Schwerpunkt und den Ebenenversatz der drei Modelle. Die Ergebnisse weisen auf keinen signifikanten Einfluss der Dunklen Materie Modelle auf räumliche Verteilungen und insbesondere flache Ebenen hin. Was das Achsenverhältnis angeht gibt es ebenfalls keinen Einfluss der Galaxienmassen.

Was die Kinematik angeht, wurden die spezifischen Drehmomente, die orbitalen Pole, der RMS Versatz zwischen Normale und den orbitalen Polen und die Dispersion der orbitalen Pole aufgenommen, um die kinematische Kohärenz der Satelliten zu bestimmen. Der RMS Versatz bestimmt, ob die Normale und die Pole (an)parallel – das heißt die Satelliten bewegen sich in einer Ebene - oder senkrecht - keine kinematische Kohärenz - zueinander stehen. Das Ergebnis was, dass die Satelliten sich nicht in der best-fit Ebene und auch nicht in einer gemeinsamen Ebene bewegen. Dieses Ergebnis ist konsistent für alle drei Dunkle Materie Modelle.

Diese Arbeit stellt keinen signifikanten Effekt der Dunklen Materie Modelle auf das Problem der Satellitenebenen, sowohl von einem räumlichen als auch einem kinematischen Gesichtspunkt, fest. In der Zukunft könnte es möglich sein, diese Arbeit auf höhere und niedrigere Galaxienmassen auszudehnen und auch andere Teilchenmassen für Dunkle Materie Kandidaten aus der Literatur zu testen. Dies könnte zu einem Modell für Dunkle Materie führen, das nicht auf Entfernungsmaßstäbe für seine Effizienz als Theorie angewiesen ist.

Contents

List of Figures

List of Tables

List of Algorithms

1 Introduction

When the scientific community was debating whether galaxies existed outside the Milky Way [4], there was a wealth of discoveries about "nebulae" being reported in the literature. Even when it was debated whether "spiral nebulae" were simply nebulae or galaxies in their own right, it was emergent knowledge that there was some missing mass in the observations of that time [5], [1], [6].

Today, evidence for dark matter comes from several astrophysical observations. From gravitational lensing observations [7], it is possible to quantify how much more dark matter there is than ordinary matter [8]. From observations of rotation curves of galaxies [9], we create a density profile for dark matter, establishing a map of where most of the dark matter is located [10], [11], [12].

1.1 Establishing the Presence of Dark Matter

Gravitational lensing is a consequence of Albert Einstein's General Relativity [13]. Objects with mass affect the curvature of spacetime, such that any object in motion must move in a way that follows this affected curvature. Light is one such object that must follow the curvature imposed by a massive galaxy as well.

Observationally, this phenomenon occurs when the light source is a distant, or *background* galaxy, bent around — *lensed* — by another galaxy in its path between us as the observers and the light source itself, making this galaxy the *foreground* galaxy, or the titular *lens* in this setup. Where on Earth, the lens relies on the refraction of light as it moves between the air and the medium of the lens, the bending of light in gravitational lensing is, of course, due to the gravity of the foreground galaxy.

As gravity is linked to mass, observational probes provide valuable insight into the mass (profiles) of galaxies. Combined with photometric studies, where radiation from luminous sources is used for mass determination, one can quantify and compare the mass of the galaxy via gravity, providing an idea of the discrepancy in the numbers yielded by the two methods. It is established today that dark matter itself exists in a quantity five times greater than ordinary (also *luminous* or *baryonic*) matter [14], [15].

Rotation curves (RCs) are an observational method where data from luminous objects — gas, stars, clusters of stars, radio sources — are gathered in terms of their distance from the galactic center and their peculiar velocity around the galactic center. Doing so results in a plot with the distance on the x-axis, and the velocity on the y-axis. This exercise is performed for objects that orbit extremely close to the galactic center, all the way out to the galactic halo at several tens to hundreds of kiloparsecs from the galactic center, encompassing the bulge and disk components as well.

The results of such observations show a deviation in the shape of the plot from the *Keplerian* curve — a plot that demonstrates Kepler's third law of planetary motion — towards a plot that either flattens out towards greater distances, or increases with the distance (Figure 1). RCs are made for several galaxies, including the Milky Way. They all more or less agree that the inner regions of a galaxy are less dominated by dark matter, with its influence increasing in the outer reaches of the galaxy [6], [1], [16], [17], [9].

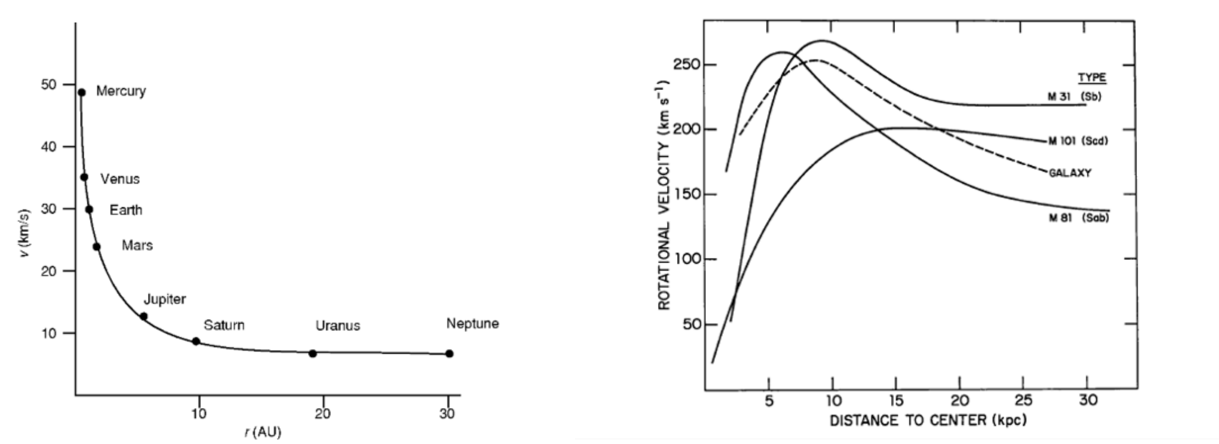

Figure 1: Left: a generic Keplerian curve that can be plotted by using the distance of the planets from the Sun on the x-axis, and their orbital velocities on the y-axis. Such a graph demonstrates Kepler's third law of planetary motion. Right: A similar exercise done for galaxies [1]. It was found that Kepler's third law is not followed here.

In order to make predictions on galactic formation and evolution, as well as (large-scale) structure formation, a mathematical profile of dark matter needs to be formulated. RCs aid in this formulation by linking the gravitation of a galaxy to the effect it has on the velocity of the objects within it, parametrized by the distance of the object to the galactic center. By linking the observables to gravitation, the mass profile (and therefore the density profile) can be derived in its mathematical form. There are several approaches to doing so [17], [12], but the consensus currently rests with the Navarro-Frenk-White (NFW) profile [10], which is derived from dark-matter-only (DMO) simulations.

1.2 Characterizing Dark Matter

A body of work establishes that dark matter is indeed something that *cannot* be detected, as opposed to a material that has simply been missing from calculations [18], and that it must be made of particles rather than being some anomaly of the force of gravitation itself [19]. Further work characterizes dark matter as cold and non-interacting [20], [21].

There were initially attempts to explain dark matter as particles or material that *was* observable, but had not been accounted for in calculations. However, they all ultimately agreed that incorporating this material into the mass profile of a galaxy did not satisfactorily cover the gap between luminous mass and gravitational (or virial) mass [22]. This line of investigation established that dark matter could not be detected by any direct detection methods: methods that depend primarily on electromagnetic radiation, which dark matter does not emit.

It is worth asking whether dark matter is indeed matter in the sense that it is made up of particles, or whether it is an anomaly of gravity as yet undiscovered. The latter school of thought formulates modifications to the theory of gravity as we know it today, making additions to Newtonian gravity, to Einstein's general theory of relativity, or indeed, formulating new models of gravity, so that it more readily explains observations. Since one of these attempts modifies Newtonian gravity, these models are called MOdified Newtonian Dynamics, or MOND [23]. The overarching claim made here is that modifying the theory of gravity eliminates the need for particle dark matter.

On the other hand, observations of the Bullet Cluster [19] and the Coma Cluster [24], made by mapping hot X-Ray gas and dark matter (via weak gravitational lensing), provide convincing evidence that the need for particle dark matter cannot be eliminated. These papers further establish that the only way dark matter can interact with baryonic matter is via the force of gravitation. Their findings also seem to suggest that dark matter seems to "direct" where ordinary matter flows, creating potential wells and filaments that attract matter gravitationally to settle where the presence of dark matter is the strongest [21], [25], [26].

Support for this argument also comes from cosmology, specifically from the studies of the cosmic microwave background (CMB) [27]. Having decomposed the CMB into a power spectrum [28], cosmologists leverage the concept of Baryon Acoustic Oscillations (BAO) [29] to determine how structures formed in the early Universe. In doing so, it is found that matter on its own interacts with itself too much — through the interactions of the Standard Model, which cause phenomena such as radiative transfer; nuclear fusion or radioactive decay; and so on — to hold any form of shape that can later become large structures. There must have been material that acted as a host for matter to gravitationally fall into, acting as potential wells of structure formation [21].

Dark matter fits this description perfectly, interacting with baryonic matter only through gravity, with two important characteristics: it must be *non-self-interacting*, and have had non-relativistic speeds during freeze-out (earning it the descriptor *cold*) so that it could remain inert during large-scale structure formation. Gravitational potential wells created by denser regions of dark matter then act as hosts for baryonic matter to fall into, forming smaller structures that evolve into galaxies, and eventually, into clusters and superclusters of galaxies.

Together, the model of dark matter we use today is of cosmological importance. This is to the extent that our current model of cosmology explicitly incorporates *Cold Dark Matter* (CDM) into its name, the ΛCDM [30].

1.3 Shortcomings of CDM

Establishing that dark matter exists raises several questions. Most pertain to the nature of dark matter and how it fits into the larger context of galaxy and structure formation, kinematics of groups and clusters, and what bearing the temperature of particle dark matter may have on its behavior, given that "cold" is an important distinction made in our current understanding of dark matter in the context of cosmology.

Indeed, no model is without its limits. In the case of CDM, these limits appear at the "local," or substructure, level, between host galaxies and their satellites [31], [32]. A few among these are the missing satellites problem, the core-cusp problem, the too-big-to-fail (TBTF) problem, and the one relevant to this work is the planes of satellite galaxies problem.

The **missing satellites problem** finds that when galaxies are evolved using ΛCDM cosmology in computer simulations, the simulations yield more satellite galaxy halos, or *subhalos* (Section 2), than are observed in their real-world analogs. This discrepancy is in orders of magnitude: simulations produce thousands of dark matter subhalos — places for potential galaxies — more than are observed around the Milky Way. This problem began surfacing in the 1990s, with [33] pointing it out in rather direct terms. Current consensus contends with this observation, however, as fainter and fainter dwarf galaxies are observed [34]. The authors in [34] also extend the missing satellites tension to environments beyond the Milky Way, where this tension is not found. The addition of baryonic physics to DMO simulations also alleviates the problem, reducing the gap between dark subhalos and luminous galaxies, and also eliminating it [32].

In Section 1.1, RCs were presented as a tool to create a mathematical profile for dark matter distribution within galaxies. These profiles fall into two broad categories, based on how they predict the density of dark matter at the center of its halo. A *cored* profile indicates that dark matter has a constant density towards the center of the halo. A *cusp* profile predicts that there is a sharp spike in the dark matter density towards the center. A discrepancy between simulations and observations is found, where simulations of galaxies yield a "cusp" profile, and observations favor a "cored" profile. This problem is summarized as the **core-cusp problem** [35].

Structure formation was highlighted in Section 1.2, with a reference to hierarchies. The **too-big-to-fail** (TBTF) problem builds on it, implying that the most massive subhalos around host galaxies should be the first to become populated by stellar mass. This line of reasoning can be followed by inferring that more dark matter implies a bigger potential well for luminous matter to fall into. This is found to be in contention with ΛCDM, as explained in [36], [37]. In [37], the authors compare theoretical predictions of ΛCDM, simulation results from Aquarius, and a compilation of observational results of the Milky Way satellite system to perform *abundance matching*, wherein the virial masses and luminous masses of observed (dwarf) galaxies are compared to their simulation analogs. Their analysis found that, in contention with predictions from ΛCDM, the most (virial) massive dwarfs did not match the most luminous dwarfs. The authors in [37] find that while many subhalos (galaxies) in simulations match the observed dwarfs around the Milky Way, these are not the same subhalos expected to host galaxies according to ΛCDM predictions. Of the three explanations proposed for this mismatch in the paper, the authors conclude that no one explanation on its own can bridge this gap between theory and observation. The argument that lends the problem its name is that massive subhalos are simply *too big to fail* at creating stars.

1.3.1 Planes of Satellite Galaxies

Reference [38] points to observational evidence that dwarf galaxies around a massive host — as in the case of our own Milky Way, the Andromeda galaxy, Centaurus A, and the Local Group — seem to arrange themselves in a relatively flat distribution. More recently, it was suggested in [39] that the Sculptor group also has such a distribution around itself. These satellite planes can be evaluated based on their thicknesses, axis ratios, and the kinematics of the constituent dwarfs and globular clusters. The deviation from a random distribution — as predicted by ΛCDM — is found to be significant, and simulations cannot reproduce these planes under ΛCDM models with statistical significance of more than a few percentage points.

The Vast POlar Structure, or the VPOS found around the Milky Way, consists of eleven of the brightest ("classical") satellites orbiting it. The observed distribution is found to only occur in $1 - 2.5\%$ of analog systems studied in simulations, when the kinematics as well as spatial distribution are considered. The Great Plane of Andromeda, or the GPoA, is a flat distribution of 15 out of the 27 brightest satellite galaxies in the system. It is recovered — in terms of position *and* kinematics — in only $0.04 - 0.17\%$ of analogous simulations. The Centaurus A Satellite Plane, or CASP, is observed at 3.8 Mpc and consists of 29 satellites. Comparing it to its simulation analogs, the CASP is recovered in 0.1% of all cases in DMO simulations, and 0.5% of the time in hydrodynamical simulations (all numbers from [38]). One of the problems, therefore, is that when all these probabilities from the simulations are combined, the product of these probabilities — which would yield the probability of observing all three systems in the same Universe simultaneously — suggests that such configurations are extremely rare. For observations and simulations that have ΛCDM as the basis for their results, this poses a question of uniqueness: *how did we end up in a Universe where all three (and perhaps more) satellite planes existed?*

To contrast, in [40], the authors report that the Milky Way plane can be explained using ΛCDM. They point to the fact that the radial distributions of the Milky Way plane are more centrally concentrated, and that the orbital kinematics of only a subset of the 11 classical satellites are consistent with a rotating plane. The authors also argue that the plane is not a permanent feature of the Milky Way satellite system. Even considering their arguments, the percentage of satellite planes found in simulations, where the criteria for the selection of Milky Way analogs are loosened based on what the authors suggest, does not exceed 2%. Further, it does not explain how or why more planes have been observed. Even if the Milky Way plane were consistent with ΛCDM, the others may not be.

This tension, explored in the present work, is termed the **planes of satellite galaxies** problem and is part of a broader study of phase-space correlations of satellite galaxies around a massive host [41]. Possible explanations for this problem come in the form of group infall, the movement of dwarf galaxies along filaments in hierarchical structure formation, accounting for hydrodynamics, and tidal dwarf galaxies. The last of these ideas requires the invocation of MOND rather than ΛCDM [38].

One of the proposed solutions is that these planes occur as satellite galaxies move along filaments in the cosmic web [38], [42], [43]. The filaments themselves are the result of matter collapse along two axes: once forming a sheet, and then forming a spine. Satellites are attracted to the nodes connected by these filaments, where a massive host resides. The most massive satellites are preferentially accreted first. This mechanism has not been found to sufficiently explain satellite planes, however, since the filaments feeding massive hosts such as the Milky Way and Andromeda are wider than their virial radii [38]. The authors argue in [42] that ΛCDM can explain the formation of satellite planes, but cannot reliably predict the amplitude and direction of the resulting anisotropy.

It may be possible that a group of satellite galaxies falls into the gravitational potential of a massive host, as suggested in the *group infall* scenario. This would explain the kinematic coherence found in satellite planes. After this accretion, the gravity of the host would dominate over the gravity between the individual group members, separating them and forming a common plane, with [44] providing observational evidence of such an explanation. Simulations of this scenario do not seem to favor this explanation, however, with [38] reporting that for the Andromeda analogs, group infall is as unlikely as finding the plane itself. Further, such an explanation only seems to work for a small number of satellites, not for as many satellites as are observed around the Milky Way and Andromeda.

Including baryonic physics in DMO simulations alleviates the other small-scale challenges to ΛCDM, and so it is reasonable to apply it here as well. However, the other small-scale challenges are more concerned with the internal dynamics of galaxies (the TBTF problem, for example, concerns the efficiency of stellar formation in massive halos), and not the orbital dynamics. On scales of hundreds of kiloparsecs to megaparsecs, where dark matter is the gravitationally dominant element, baryonic physics does not have a significant impact [38].

Finally, it may be possible that tidal disruptions caused the progenitors of present-day satellites to be "stripped," creating smaller dwarfs that rotate in the same direction as the progenitor did. Observational and simulation corroboration are provided for this scenario in [45]. This explanation accounts for spatial and kinematic coherence at once; however, observed satellite galaxies are more dark matter dominated than what this scenario suggests. Further, such a scenario is less plausible in ΛCDM than it is in a modified version of it, or even in a modified gravity model which eliminates the need for dark matter entirely [38].

The solution explored in this work is to alter the underlying model of dark matter altogether. Using simulation data from AIDA-TNG (Section 2) [46], a warm dark matter (WDM) model is evaluated, along with a self-interacting dark matter model (SIDM). These models are elaborated upon in the following section.

1.4 Simulations and the Present Work

Simulations occupy an important space in cosmological research. They allow us to surpass mass, distance, and time scales that would otherwise be incomprehensible to the human mind. Further, they provide an arena for "experimentation": observations are constrained to snapshots at one time of one specific galaxy of one specific type (there is only one Milky Way galaxy, for example, just as there is only one Andromeda galaxy), and simulations allow for reproducibility of specific initial conditions. Thus, they are an important tool for testing theoretical predictions, for improving constraints on current models, and finally, for providing observables that can be further tested in our own Universe.

Another advantage of simulations is that they allow for changes in fundamental laws of physics. What if dark matter were not *cold*? What if it did interact with itself? What changes, if any, would it bring about in the observables? Would it solve some of the problems presented in Section 1.3? **What would changing the dark matter model do to the problem of the planes of satellite galaxies?**

In order to explore the research question, I first establish the dark matter models explored in this paper.

1.4.1 Cold Dark Matter (CDM)

This is the most thoroughly explored model of dark matter, which finds consensus in the current model of cosmology. Particles of cold dark matter must be massive, non-relativistic at early cosmological timescales, and non-self-interacting. This type of dark matter can then form gravitational potential wells for baryonic matter to coalesce into galaxies, giving rise to the observed large-scale structure of our Universe. A review of CDM pertaining to galaxy formation can be found in [47].

Several particle candidates have been proposed and are being explored as potential constituents of cold dark matter. These include Weakly Interacting Massive Particles (WIMPs) and sterile neutrinos [48]. This work falls under astroparticle physics, where researchers are anticipating the expansion of the standard model of particle physics with the discovery of non-standard particles [49].

1.4.2 Warm Dark Matter (WDM)

The motivation to formulate a particle that was relativistic before matter-radiation equality, and non-relativistic thereafter, comes from the clustering observed at small scales, the core/cusp problem, and the missing satellites problem [50]. These particles are subject to free streaming and suppress the formation of low-mass galactic-scale halos [46]. The absence of the low-mass halos solves the missing satellites problem, as the low-mass and early relativistic nature of the WDM particle suppresses small-scale structure formation. Within the halos themselves, it was found that WDM reduced the severity of the core-cusp problem, and their radial extents increased [50].

The data analyzed in this work examine WDM with a particle mass of 3 keV (abbreviated WDM3), which lies at the observational limit of credibility. It has been "ruled out by combined analysis," meaning that the combination of observational probes does not favor this model, but individual probes still allow it [46]. The authors of [46] also assess particle masses of 1 keV and 5 keV in addition in 3 keV. The 3 keV case is useful to contextualize the authors' findings, since there is pre-existing literature on this model of warm dark matter, and AIDA-TNG is the first simulation that assesses dark matter models on a cosmological scale.

1.4.3 Self-Interacting Dark Matter (SIDM)

If one does away with the assumption that dark matter particles cannot interact among themselves, the door to self-interacting dark matter models (SIDM models) is opened. It was proposed to solve the core-cusp and missing satellites problem [51]. With this shift in the perception of dark matter interactions, it is now possible to treat them using particle physics principles in terms of energy/momentum transfer, with the caveat that the exact nature of the interaction remains unknown.

The AIDA-TNG simulation focuses on the model advantage that particles can now transfer energy and momentum amongst themselves, meaning that halos can now be "heated". As in particle physics, there is now a cross-section of interaction σ/m_χ to be considered, where m_χ is the mass of the hypothetical dark matter particle. This quantifies the probability that two SIDM particles will interact with each other [46], [51]. AIDA-TNG explores two possibilities: that the cross-section is a constant at $\sigma/m_\chi = 1\text{cm}^2\text{g}^{-1}$, and that the self-interactions are elastic in nature and dependent on the velocity of the particles. The former of these is explored with the abbreviation SIDM1, while the latter, also relevant to this work, is abbreviated as vSIDM, with the v standing for velocity.

1.5 Present Work

In this thesis, I explore the planes of satellite galaxies problem as described in Section 1.3.1. I process data from the AIDA-TNG simulation, a derivative of the Illustris-TNG simulation

(Section 2), to fit planes through satellite galaxy distributions around Milky Way analogs in the data. The models of dark matter under consideration are CDM, vSIDM, and WDM3. The planes are assessed for their thicknesses, axis ratios, and radial extents. The host mass and kinematics are also taken into consideration, in addition to the isotropic cases derived from the models. The goal of the research is to assess whether any one of these models produces satellite planes with more significance than the others; in other words, whether the formation of satellite planes depends on the model of dark matter employed.

Given the recency of the AIDA-TNG research, and the fact that AIDA-TNG is the first time alternative dark matter (ADM) models have been examined in cosmological simulations, this thesis marks a first attempt at analyzing this data in the specific context of satellite planes.

2 Data

The data for this work comes from AIDA-TNG [46], which is based on the numerical methods and implementations employed in Illustris-TNG [3].

Illustris-TNG is a suite of cosmological simulations that incorporates ΛCDM cosmology along with baryonic physics (fluid dynamics, plasma physics, magnetic processes) in order to simulate the large-scale structure of our Universe [52]. It is based on the moving-mesh AREPO code [53], with particles from stars and stellar winds, black holes (treated as particles themselves), dark matter, and tracers incorporated into the implementation. A tree-particle mesh algorithm implements (self-)gravitation.

There are three box sizes released for this simulation, with periodic boundaries [54] of 50 Mpc (TNG50), 100 Mpc (TNG100), and 300 Mpc (TNG300) [52]. There is a tradeoff between box size and spatial resolution: where TNG50 is suitable for studying individual galactic processes such as star formation and feedback, TNG300 is more suited towards studies of the large-scale structure.

To implement galaxy formation, models describing star formation, stellar evolution, black hole formation and evolution, and feedback mechanisms are taken into consideration. Where the processes are too complex, given the resolution of the simulation, an idealized version of the physics is used [55]. As an example, the model for galaxy formation used in Illustris-TNG incorporates star formation and evolution, chemical enrichment, gas cooling, galactic outflows due to stellar feedback, supermassive black hole formation, growth, and feedback. For star formation, a stochastic process has to be introduced if the gas density in a region goes above a specific threshold. In stellar evolution models, wind ejection only from the asymptotic giant branch stars is considered, and not from other stellar evolutionary phases [52].

The motivation for these simplifications is to reduce the computational load for the AREPO code, where memory space is compromised in favor of time efficiency: in other words, the code uses a large memory space to run in shorter spans of time [53]. This moving-mesh code is favored for fluid dynamics, which includes gas flows, heating or cooling, and feedback processes. Further applications also implement magnetohydrodynamics, providing a full picture of astrophysical processes ranging from stellar formation to galactic mergers. Its advantage lies in the Voronoi mesh, where each particle exerts influence (for example, through gravitation) in a defined polygonal region (the number of sides of this polygon depends on the number of particles in the vicinity of the influencing particle). This polygonal region around each particle is redefined every time a particle is displaced from its position, forming a lattice of points [53].

Further, the suite of simulations includes runs that test the gravity of dark matter only (the DMO runs), as well as versions that include baryonic physics to provide a full picture of the relevant physical processes. The latter are aptly named Full-Physics (FP) runs. The suite of simulations begins with its initial conditions at redshift $z = 127$ and evolves it to the present day at $z = 0$.

To identify dark matter halos, the Friends-of-Friends (FoF) algorithm [52], [56] is used. This algorithm identifies regions of high density of dark matter. In this way, the FoF algorithm identifies *halos*. An algorithm used extensively in the Illustris-TNG suite of simulations, the SUBFIND algorithm [57], identifies "locally overdense, self-bound particle groups" and labels them as *subhalos*. This algorithm is applied to an FoF group (halo), finding *locally* overdense regions therein, creating a "halos within halos" hierarchy. These subhalos are interpreted to be galaxies. Thus, the structure can be read as a cosmological simulation box (with a given periodic boundary) where large-scale structure is determined by the clustering of halos, which contain smaller regions of overdensities known as subhalos, which themselves contain (satellite) galaxies. The host galaxy is understood to be in the *central* subhalo.

AIDA-TNG is a "derivative" of the Illustris-TNG simulations [52] in the sense that it uses the same code, but evolves it under different models of dark matter. The simulation uses the box sizes of TNG50 and TNG100, where the focus of this work is on the 50 Mpc box due to its higher resolution (compared to TNG100). Within this 50 Mpc box, the authors highlight two runs: the 50/A and 50/B. These letters refer to the resolution of the box in the Illustris-TNG framework: "A" refers to the TNG50-2 run, while "B" refers to the TNG50-3 run. Between the two, 50/A has more resolution than 50/B [46]. The data for this project is taken from the AIDA-TNG 50/A run, meaning that the size of the periodic box is 51.7 Mpc, with a resolution and initial conditions equivalent to those of the TNG50-2 run. Reference [46] reports the spatial resolution of this run to be 570 pc; the dark matter particle mass resolution is $4.3 \times 10^6 M_\odot$ for the DMO run or $3.6 \times 10^6 M_\odot$ for the FP run. For this project, the data for the FP run were accessed.

The data for this project were accessed at snapshot 99, corresponding to redshift $z = 0$ and scale factor $a = 1$ [3]. This set includes data for CDM, vSIDM, and WDM3 [46].

The results are gathered and stored in the same field names and data types as the Illustris-TNG data, making documentation and data specifications readily accessible. The fields described in the documentation [3] are used to (a) filter the data as in Figure 2, (b) perform a plane-fitting analysis (Section 3), and (c) create output plots (an example can be seen in Appendix C). A full table describing the fields of data accessed is presented in Appendix B.

The simulation data is implemented in Python as a nested dictionary in column-major format. The full dataset is pared down to Milky Way (MW) analogs using the field **['halos']['Group_M_Crit200']**, which is the virial mass M_{200} of a galaxy, and constraining it to a reasonable MW-like mass range ($0.8 - 3 \times 10^{12} M_\odot$: [58], [59], [60]). Within the MW analogs, the subhalos are then pared down on the basis of stellar mass (M_*) (**['subhalos']['SubhaloMassType']**[:, 4] > 0) and dark matter dominance (**['subhalos']['SubhaloMassType']**[:, 1]/**['subhalos']['SubhaloMass']** > 0.8). To determine the dark matter fraction, [61] reports the dark matter mass of the Large Magellanic Cloud (LMC), while [62] reports the total mass of the LMC. The fraction yields $\sim 94\%$, but I was lenient in my limits to allow for lower-mass subhalos as well.

It is then important to find which subhalos belong to which halo to establish a host-satellite system, requiring a cross-match between the **halos** and the **subhalos** catalogs. This is achieved by using the field **SubhaloGrNr** within **subhalos**, indexing a halo within the **halos** table. In this analysis, the group number takes on the role of a primary key in identifying systems of particular interest. The number of satellites per halo is defined with the variable N_{sat}.

Further, in order to calculate the plane properties, an additional constraint is put on the subhalos such that no subhalo within 10 kpc of the central subhalo (**['halos']['GroupFirstSub']**) can be selected to ensure that no disk fragments enter the dataset. For reference, the closest dwarf galaxy to the Milky Way was found at $\sim 12 - 13$ kpc from the galactic center [63]. Of the final cut, plane fitting is performed using only the top ten luminous satellites (sorted on M_*), as these are the ones available for our observation in a real-world setting. Doing so also equalizes the number of satellites per system for a fair comparison across models, reducing the look-elsewhere effect. The process is explained with a flowchart (Figure 2), also quoting the data sizes at the end of each cut.

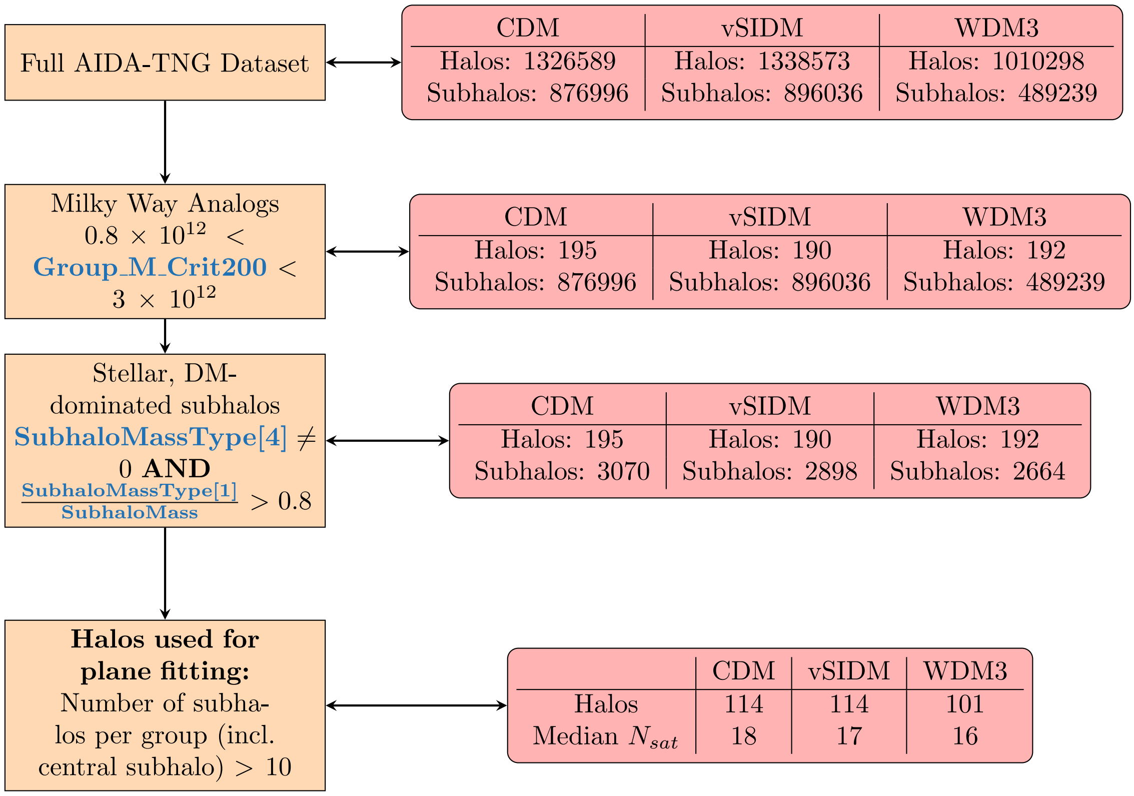

Figure 2: A flowchart of the data selection process for Milky Way-like hosts with luminous, dark-matter-dominated satellites.

The resulting medians and cumulative distribution functions are discussed in Section 4.1, where a full summary of the data is presented.

3 Methods

3.1 Geometry and Centering

According to the data arrangement of the AIDA-TNG simulation, each halo has several subhalos, with one galaxy assigned to one subhalo. In this way, a *halo* refers to a system of one central galaxy with several satellites around it.

However, it can be (and almost always is) the case that the central subhalo — the host galaxy — is *not* at the geometric center of the distribution within a halo (see Figure 11, left). In this case, it helps to compute the geometric center (centroid) of the distribution. Doing so gives rise to two geometric orientations.

On the one hand, one can consider the central subhalo to be the center of the distribution, with the other subhalos being the satellite galaxies orbiting around it. In this case, the simulation coordinates need to be converted to *host-centered (hc)* coordinates and must pass the periodic boundary condition (PBC) [54]. In Equation (1), the centering procedure is shown for a vector $\mathbf{r}$ given a periodic box size L.

$$\mathbf{r}_{\text{hc}} = \mathbf{r} - \mathbf{r}_{host} \tag{1}$$

if (a) $\mathbf{r}_{\text{hc, i}} > L/2$ or (b)$-\mathbf{r}_{\text{hc, i}} < -L/2$ **then**

(a) New $\mathbf{r}_{\text{hc, i}} \leftarrow \mathbf{r}_{\text{hc, i}} - L/2$

(b) New $\mathbf{r}_{\text{hc, i}} \leftarrow \mathbf{r}_{\text{hc, i}} + L/2$
for i being the individual component of the vector $\mathbf{r}_{\text{hc}}$.

The periodic boundary condition is applied iteratively until all components of $\mathbf{r}_{hc}$ are within the specified $L/2$ box size.

It is now convenient to compute the centroid of the host-centered points following this procedure. The centroid so computed will be positioned relative to the central subhalo, which allows us to calculate the centroid offset:

$$\begin{aligned} \mathbf{c} &= \bar{\mathbf{r}}_{\text{hc}} \\ d &= |\mathbf{c}| \end{aligned} \tag{2}$$

When we consider the central subhalo to be at the origin and center the points accordingly, we make the assumption that it is at rest, and the other satellites are moving relative to it. In the simulation, however, every subhalo has a peculiar velocity v. So, if we are to consider the rest frame of the central subhalo, the velocities of the other subhalos must be computed relative to the host.

$$\vec{v}_{rel} = \vec{v}_{subhalo} - \vec{v}_{host} \tag{3}$$

The Galilean transformation is used here rather than the relativistic one because the peculiar velocities used in this work are non-relativistic (in the hundreds of km/s range). We thus have a set of coordinates (Equation 1) and relative velocities and can define some orbital properties, such as the specific orbital momentum $\vec{h}$ and orbital pole $\hat{h}$.

$$\begin{aligned} \vec{h} = \frac{\vec{L}}{m} &= \mathbf{r}_{\text{hc}} \times \vec{v}_{rel} \\ \hat{h} &= \frac{\vec{h}}{|\vec{h}|} \end{aligned} \tag{4}$$

In Sections 3.3 and 4.1, the relevance of these quantities in addition to plane fitting (Section 3.2) is discussed.

On the other hand, coordinates can also be centered around the centroid $\mathbf{c}$. In this frame, the central subhalo is also offset from this centroid. The reason this makes sense in geometry is that the position vectors $\mathbf{r}_{\text{hc}}$ have already been corrected for the periodic boundary, which means they can now be used for calculations involving differences between two vectors without loss or over-correction of information. It is now reasonable (and convenient) to perform the following operation:

$$\mathbf{r}_{cc} = \mathbf{r}_{\text{hc}} - \mathbf{c} \tag{5}$$

I use the term *centroid-centered coordinates* (or *frame* to replace *coordinates*) to refer to $\mathbf{r}_{cc}$.

The host-centered reference frame is the frame used in observations, as we observers reside within the MW and look *outwards* towards our own satellite system. The centroid-centered frame, in conjunction with the host-centered frame, provides a stable point relative to which all galaxies, including the host, can be studied. (When studying the evolution of a satellite system, it is possible that the centroid itself shifts given the motion of the galaxies. However, since I only look at one snapshot here, the centroid can be considered stable.) Assessing the centroid-centered frame provides insight into the distribution of galaxies: more distant subhalos skew the centroid offset.

The INERTIA_TENSOR() function (Section 3.2) operates twice on every system: once using the host-centered coordinates, and once using the centroid-centered coordinates.

3.2 Plane Fitting Functions

The function INERTIA_TENSOR() makes use of the tensor of inertia for a given distribution of points in order to identify the principal axes of the point cloud distribution.

The idea of the tensor of inertia is borrowed from rigid body dynamics, where it expands the concept of the classical moment of inertia:

$$\{\mathbf{I}\} = \begin{bmatrix} I_{xx} & I_{xy} & I_{xz} \\ I_{yx} & I_{yy} & I_{yz} \\ I_{zx} & I_{zy} & I_{zz} \end{bmatrix} = \begin{bmatrix} M \times (y^2+z^2) & M \times x \times y & M \times x \times z \\ -M \times x \times y & M \times (x^2+z^2) & -M \times y \times z \\ -M \times x \times z & -M \times y \times z & M \times (x^2+y^2) \end{bmatrix} \tag{6}$$

Where M in this specific case is taken to be the mass of the individual subhalos, and x, y, and z refer to the coordinates of *one* subhalo, centered around its host (or the centroid, depending on the frame of reference as described in the previous section). In the computational implementation presented in this thesis, *equal weighting* is assigned for all subhalos, so that the more massive satellites do not dominate the spatial distribution for which we want to find a plane. This aligns with observations of the planar structure around the Milky Way [64], which is not dominated by the LMC, the most massive of the Milky Way's satellites.

Algorithm 1 returns the tensor of inertia in its diagonalized form such that the principal axes are readily extractable. The calculations that follow — axis ratios, RMS heights about each axis — are then more conveniently returned to the user for further testing. The idea here is that the major, minor, and intermediate axes are based upon the spatial distribution of the points about them. The major axis is the axis with the lowest eigenvalue of the inertia tensor, and in rotational dynamics would refer to the axis about which the moment of inertia is the lowest. On the other hand, the minor axis corresponds to the largest eigenvalue of the inertia tensor; in rotational dynamics, this is the axis about which the moment of inertia is maximized.

The reason we are interested in finding the *minor* axis, therefore, is that for a large moment of inertia, the points must be spatially distributed in a way that maximizes their distance from the axis: the orientation with the largest "spread" *around* the minor axis. The direction of the minor axis in this case is orthogonal to a planar distribution. This is exactly what is needed for the equation of a plane (Equation 7).

$$Ax + By + Cz = D \tag{7}$$

Where A, B, and C are respectively the x-, y-, and z-components of the minor axis. In this document, A, B, C, and D together are referred to as the *plane coefficients*.

To implement these calculations in a program, a function loops over a distribution of points arranged in an $N \times 3$ array, where N is the number of points in the distribution. In doing so, the tensor of inertia is newly generated at each iteration, calculating the eigenvalues and eigenvectors of the new tensor to determine the major, minor, and intermediate axes.

While developing Algorithm 1, it seemed that the INERTIA_TENSOR() function initially returned values that did not visually match the plane that has been fit through the cloud of points. Therefore, it was necessary to run tests on the return values of the function to ensure it behaved as expected. To do this, I set up two thousand artificial planes and introduced a thickness Δ_{rms} in the form of a standard deviation.

3.2.1 Random Generation of Points

To create an artificial plane that may be considered analogous to the Milky Way system, I begin by determining the direction in which I would like the plane to be oriented. To do so, we require the plane coefficients A, B, and C (Equation 7). D is determined by using the centroid of the subsequent randomly generated points. With this comes the implicit assumption that all coordinates will be centered around the origin. The plane coefficients are generated randomly in the code implementation. These coefficients are normalized so that they form a unit vector in the desired direction.

To generate the random points, we must think of the Milky Way system in cylindrical polar coordinates.

$$\begin{aligned} x &= r\cos\theta \\ y &= r\sin\theta \\ z &= z \end{aligned} \tag{8}$$

Here, r is analogous to the radial extent of the Milky Way system, taken to be 250 kpc [38]. However, to ensure that the randomly generated points lie *within* this upper limit, and not only on a circle defined by $r = 250$ kpc, this value is also randomly generated between 20 (the closest dwarf galaxy to the Milky Way is referenced in [63]) and 250 (following the radial extent of the satellite plane of the Milky Way, [38]). The angle θ is randomly generated between 0 and 2π radians to fully encircle the planar space around the origin (where we imagine the Milky Way to be). This generation of r and θ makes up the random x- and y-coordinates. The process is repeated 27 times in this work (as 27 satellites were counted in [65]), but this number can be adjusted, e.g., to only account for the eleven "classical" satellites or to count a larger number of satellites [66].

For the z-coordinate, I introduce a standard deviation which acts as the "thickness" of the plane. I expect this thickness to correlate with other values (e.g., RMS heights) at the end of the inertia tensor tests, which will determine how well the inertia tensor function works.

Given the intended plane coefficients and a random point cloud distribution in the $x-y$ plane (where $z = [0, 0, 1]$ is the normal to the plane), the latter must now be rotated so that it matches the orientation determined by the plane coefficients. To do so, I employ the Rodrigues rotation formula [67].

$$R = \mathbf{I} + K\sin\theta + K^2(1-\cos\theta) \tag{9}$$

This formula yields a rotation matrix that can be multiplied by the randomly generated points to form the intended plane. Here, $\mathbf{I}$ refers to the 3×3 identity matrix and K refers to the K-matrix that can be calculated using Equation 10.

$$\begin{aligned} \mathbf{R_{rot}} &= \mathbf{n} \times [0,0,1] \\ \hat{\mathbf{R}}_{rot} &= \mathbf{R_{rot}}/|\mathbf{R_{rot}}| \\ \theta &= \arccos(\mathbf{n}\cdot[0,0,1]) \\ K &= \begin{bmatrix} 0 & -\hat{\mathbf{R}}_{rot,z} & \hat{\mathbf{R}}_{rot,y} \\ \hat{\mathbf{R}}_{rot,z} & 0 & -\hat{\mathbf{R}}_{rot,x} \\ -\hat{\mathbf{R}}_{rot,y} & \hat{\mathbf{R}}_{rot,x} & 0 \end{bmatrix} \end{aligned} \tag{10}$$

Equation 10 determines the axis about which the points must be rotated, from the z-axis to the intended orientation given by the normalized plane coefficients (determined by $\mathbf{R_{rot}}$); next, it determines the angle of rotation θ as required in Equation 9. Finally, the components of the normalized rotation axis, $\hat{\mathbf{R}}_{rot}$, compose the K-matrix given in Equation 10.

R as obtained from Equation 9 is then multiplied by the randomly generated points to create the artificial plane, with randomized plane coefficients and random introduced standard deviation (thickness), that will test the working of the inertia tensor function. The computational implementation of Equations 7, 8, 9, and 10 is outlined in Algorithm 2, Appendix A.

This random generation of points is followed 2000 times. Each coefficient A, B, and C is chosen in the interval $[1, 21)$ so that there are 20 possibilities for each variable, and $20 \times 20 \times 20 = 8000$ possible combinations that can be tested. (There is no reason for choosing this interval beyond having "readable" plane coefficients; the tests that follow will reproduce the values returned by the computational implementation regardless of what plane coefficients are chosen, or whether or not negative values or floating point values are included.) This ensures that there will be no repetition of an A, B, C combination over the 2000 trials. They are also normalized.

$$\mathbf{n} = A\hat{x} + B\hat{y} + C\hat{z}$$
$$\hat{\mathbf{n}} = \frac{\mathbf{n}}{|\mathbf{n}|} \tag{11}$$

The artificially chosen thickness is also randomly generated at each trial such that it is a floating point number in the interval $[0, 100]$. This range reflects the typical RMS heights obtained in the simulation data.

Once the points are randomly generated, their centroid is calculated and the points are centered around the centroid (Equation 5). The value of D for the intended plane is calculated replacing x, y, and z in Equation 7 by x_c, y_c, and z_c. The inertia tensor is implemented on these centered vectors, and here begins the testing. This value of D is also normalized using the magnitude of the normal $|\mathbf{n}|$ (Equation 11).

From the inertia tensor function, I extract the following: the unit vector of the normal to the plane $\mathbf{n}$, the minor-to-major axis ratio c/a, the intermediate-to-major axis ratio b/a, and the RMS heights along the minor axis Δ_{rms}^{TOI}. The value of D for the plane coefficients returned by the inertia tensor function is calculated the same way it was done for the plane coefficients of the intended plane.

Now, I have a value of Δ_{rms} returned by the inertia tensor function, which was calculated for the points to the plane fit by the function. I need a value for Δ_{rms} that is calculated for the heights of the points to the plane that was originally intended. To do so, I follow Equation 12 for each vector $\mathbf{r}$ that was generated for the given iteration.

$$\Delta = \frac{(\hat{\mathbf{n}}_{intended} \cdot \mathbf{r}) - D_{intended}}{|\mathbf{n}_{intended}|}$$
$$\Delta_{rms} = \langle \Delta^2 \rangle \tag{12}$$

In order to evaluate whether the intended plane and fit plane overlap, I check whether they are parallel to each other, and do so by looking for the angle between the two planes. I would like for this value to be close to 0 to ensure that the planes are parallel. The plane coefficients for parallel planes are equal.

$$\theta = \arccos(\hat{\mathbf{n}}_{intended} \cdot \hat{\mathbf{n}}_{TOI}) \tag{13}$$

Algorithm 3, Appendix A describes the computational implementation of the procedure. All quantities are recorded in an output file.

From the output files, the relevant variables are extracted and processed to plot the quantities against each other. The results of this testing confirm the robustness and functionality of INERTIA_TENSOR().

3.2.2 Results from Function Tests

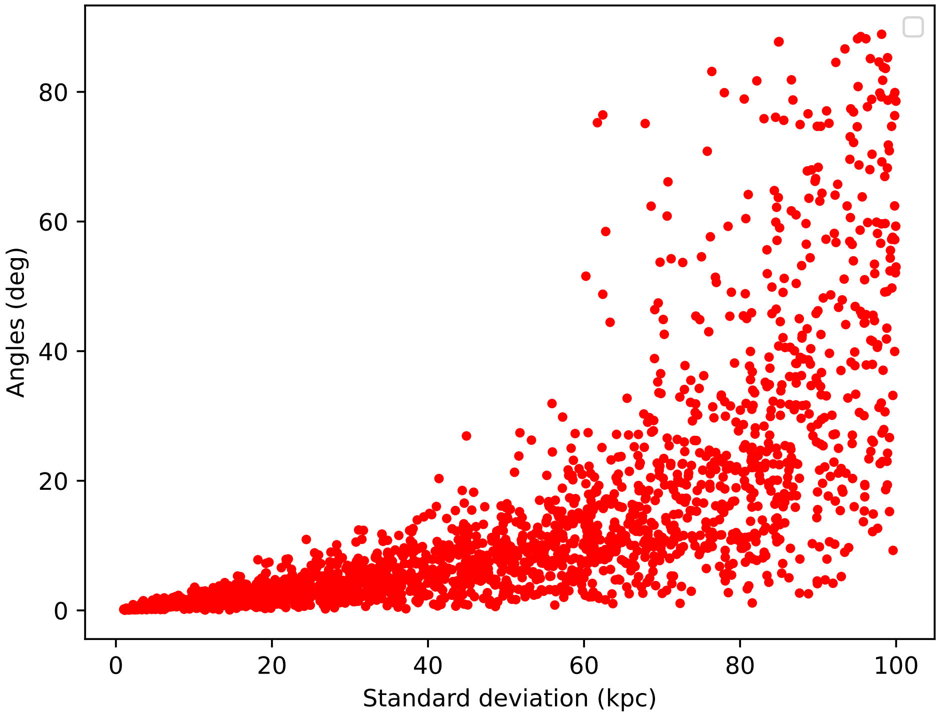

Figure 3: The input standard deviation, introducing a plane height (shown here on the x-axis), is treated as an independent parameter, introducing artificial errors while generating points that supposedly lie on a plane. The output yields two planes: first, the intended plane; and second, the plane fit using the tensor of inertia. The angle between these two planes is reflected on the $y-$ axis, in degrees.

It is apparent from Figure 3 that the angle between the intended plane and the fit plane θ increases with increasing standard deviation (which I compare with the values Δ_{rms}^{calc} and Δ_{rms}^{TOI}). This is due to the fact that the drawn sample only contains 27 points in increasingly thicker planes — at greater standard deviations, a "thick" plane of 27 points cannot easily be distinguished from a regular isotropic point cloud distribution: it is more difficult to define a plane on highly scattered points as opposed to a relatively narrow distribution. This can be rectified by increasing the number of points. Figure 3 shows that with increasing standard deviations, the plane coefficients returned by the INERTIA_TENSOR() function deviate significantly from the intended plane coefficients, resulting in fit planes that are at an incline to the artificial plane that was the starting point.

However, this does not affect the efficiency of the function itself. There is a tight correlation between the RMS heights calculated by the INERTIA_TENSOR() function (Δ_{rms}^{TOI}) and the minor-to-major axis ratio (c/a) as seen in Figure 4.

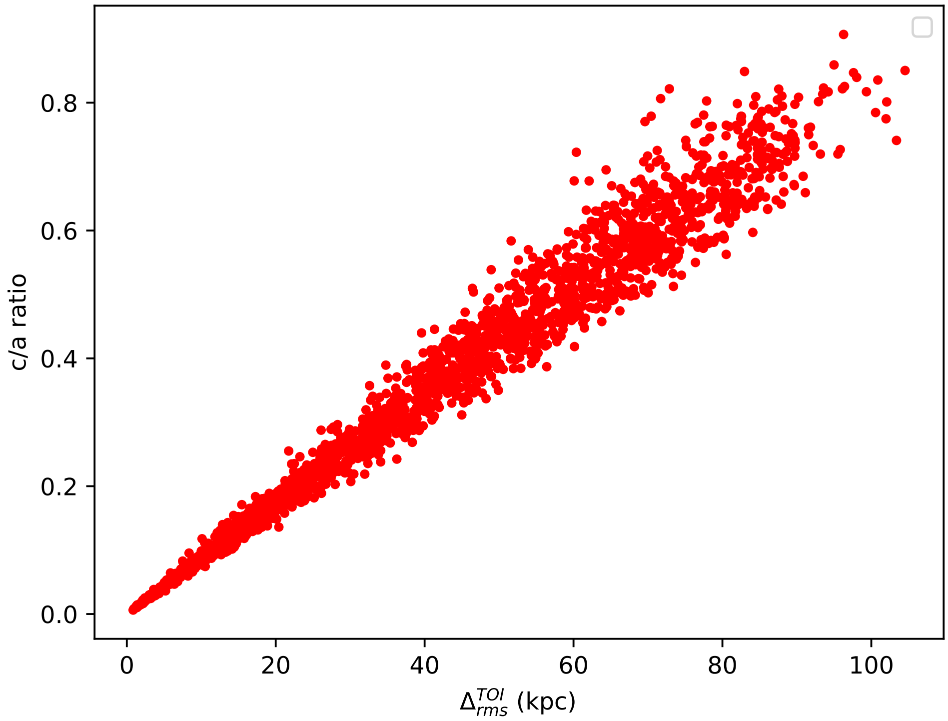

Figure 4: The INERTIA_TENSOR() function measures, among other things, the Δ_{rms}^{TOI} of the points from the best-fit plane, and the ratio of the RMS heights as measured from the minor axis compared to the RMS heights as measured from the major axis. This is what defines the c/a ratio, or simply, the minor-to-major axis ratio.

The scatter increases with increasing standard deviation in most cases, for the same reason as described for Figure 3. Figure 5 is the graph of Δ_{rms}^{TOI} as it varies with the input standard deviation.

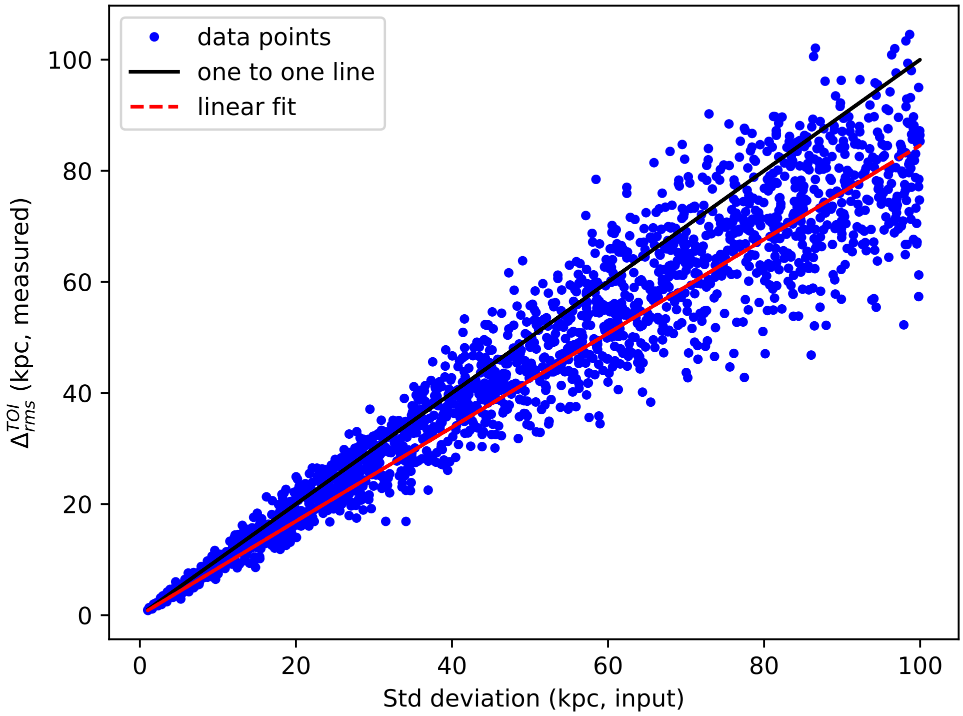

Figure 5: The introduced Δ_{rms} (standard deviation) plotted against the Δ_{rms} measured by the TOI function begins to show a scatter. However, a linear fit to the plot shows that $\Delta_{rms}^{TOI} < \Delta_{rms}^{input}$.

It is notable in this case, however, that the scatter remains *below* the one-to-one line. A linear fit shows the slope to be 0.8456 (red line, Figure 5). The INERTIA_TENSOR() function is not constrained by specific plane coefficients (as in the case of generating random points, where I generate random points on an *input* plane). Therefore, it is free to fit a plane that minimizes Δ_{rms}, and the output yields a smaller plane thickness than the input standard deviation.

In contrast, when one plots the correlation between the RMS heights returned by the INERTIA_TENSOR() function (Δ_{rms}^{TOI}) and the RMS heights that were calculated for the *input* plane (Δ_{rms}^{calc}), the result is Figure 6.

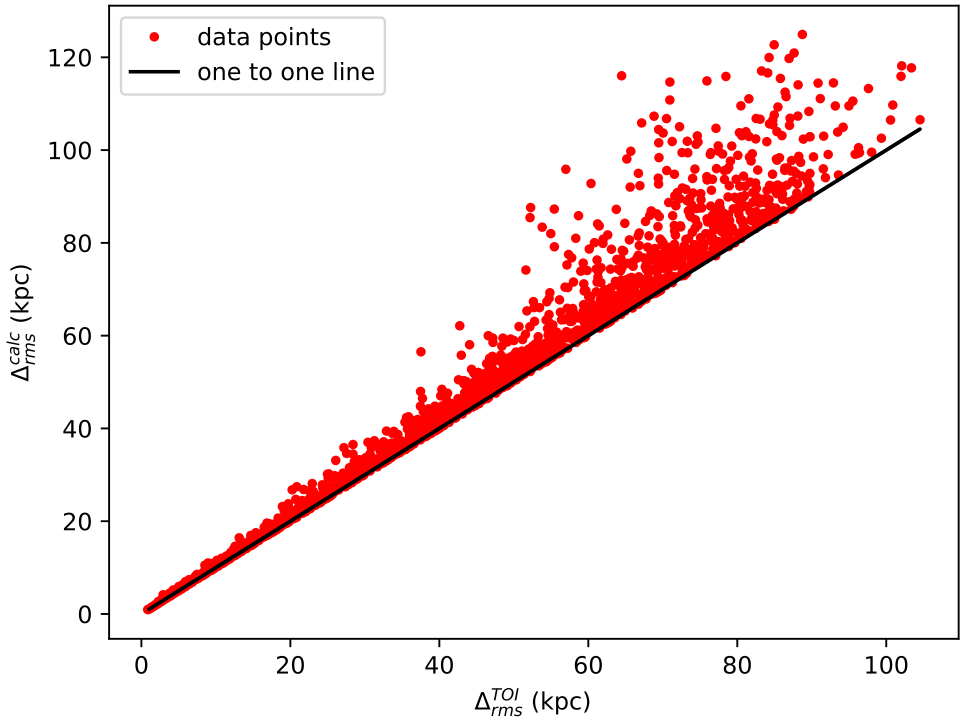

Figure 6: Δ_{rms}^{TOI} as measured by the TOI function (output) plotted against the Δ_{rms}^{calc} calculated within the code for the input plane. The image shows a clear one-to-one line; however, $\Delta_{rms}^{TOI} < \Delta_{rms}^{calc}$.

In Figure 6, the scatter still increases for higher values, but Δ_{rms}^{TOI} is always *lower* than the Δ_{rms}^{calc}, calculated for the input plane. That the INERTIA_TENSOR() function returns a smaller Δ_{rms} than the input standard deviation (or even the in-program calculations of Δ_{rms}), when it is not constrained by plane coefficients, indicates that the function is operating as intended. This is again a result of the fact that the best-fit plane, when not constrained by input plane coefficients, will always work with numbers that *minimize* any measure of Δ_{rms}. This also means that the best fit may return a value smaller than the input.

Comparing the variation of the calculated Δ_{rms} of the intended plane with increasing standard deviation (introduced while generating random points) shows a fairly symmetric scatter about the one-to-one line, as in Figure 7.

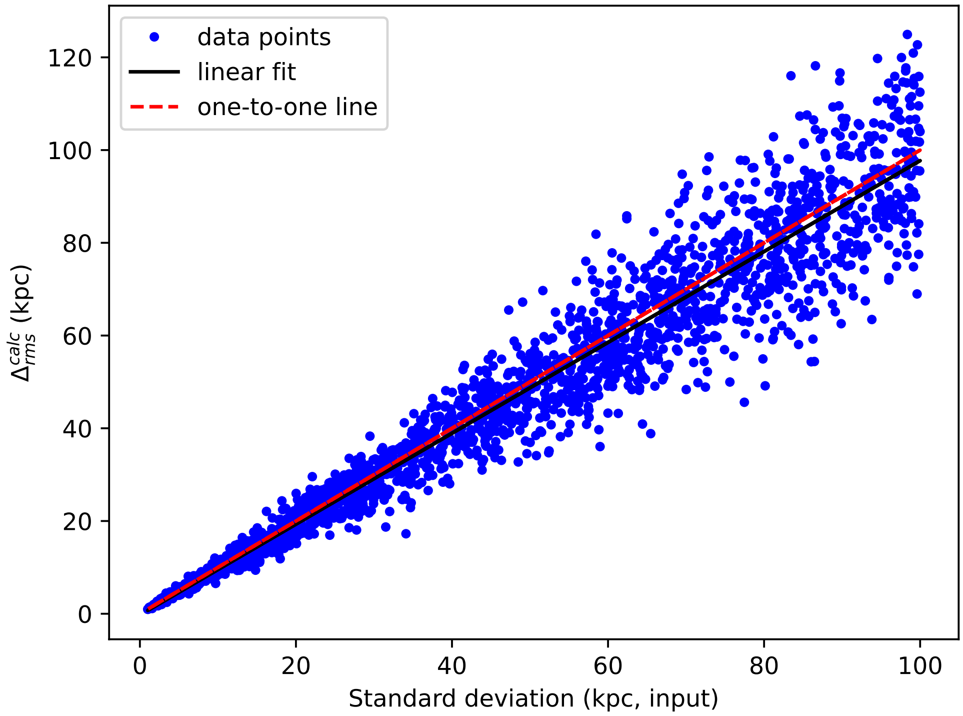

Figure 7: Comparing statistics for the intended plane: input random standard deviation when generating points on a plane (x-axis of plot) versus the Δ_{rms} measured for the same plane after the plane generation, calculated using the plane coefficients determined randomly for each run (y-axis). The two are nearly equal about a line of symmetry at ~ 1 (black line).

Performing a linear fit on this data, the slope was found to be 0.9799. Despite the noticeable scatter, the over- and underestimations may cancel each other out. As expected, the Δ_{rms}^{calc} correspond extremely well to the respective standard deviations that were artificially introduced into the intended planes.

3.3 Application to AIDA-TNG Simulation Data

Having confirmed that the tensor of inertia is robust and consistent, and having defined two coordinate centering frames, plane fitting for the satellite systems of AIDA-TNG 50/A resolution introduces the variables summarized in Table 1.

Satellite System Property	Meaning	Units
$\Delta_{rms,c}$	RMS heights in the centroid-centered frame	kpc
$\Delta_{rms,h}$ or simply Δ_{rms}	RMS heights in the host-centered frame	kpc
d	Centroid offset, the distance of the geometric center of the distribution from the central subhalo	kpc
$d_\perp$	Plane offset, the perpendicular distance of the host halo from the best-fit plane in the centroid-centered frame	kpc
θ	Angle between the plane fit in the host-centered frame and in the centroid-centered frame	deg
R	RMS radial extent (defined only for the host-centered frame)	kpc
θ_{rms}	The RMS angle of the unit vector of specific angular momentum against the plane normal	deg
$\Delta_{sph}(k)$	Orbital pole dispersion, the RMS scatter for the k most concentrated orbital poles. For the present work, $k = 10$, or the full set of satellites. In the rest of the work, this quantity is simply referred to as Δ_{sph}.	deg

Table 1: Summary of measured quantities in plane fitting analysis (See Appendix B for a full, comprehensive list.)

For easier interpretation of the results, the masses and distances are converted from comoving coordinates ($10^{10}M_\odot/h$, $ckpc/h$) to present-day coordinates ($M_\odot$, kpc).

$$\begin{aligned} M_{present} &= M_{simulation} \times 10^{10}/h \\ r_{present} &= r_{simulation} \times a/h \\ \text{Scale factor } a &= 1 \text{ for redshift } z = 0 \\ \implies r_{present} &= r_{simulation}/h \end{aligned} \tag{14}$$

The value of h is taken at 0.6774 in accordance with the parameters used in the AIDA-TNG simulation [46], adopted from Illustris-TNG [52] and ultimately from the *Planck* mission [68]. I note the difference between the vectors $\vec{h}$ and $\hat{h}$ in Equation 4 and the h in Equation 14: the latter, without the overhead arrow (or hat), is the reduced Hubble constant.

On a structural level, there were three models to be analyzed: CDM, vSIDM, and WDM3. The plane fitting procedure to be followed and the outputs to be recorded followed a common pattern, giving rise to the need for a common Python library that could be imported into each analysis file. I thus created a user-defined library that could be imported across all three files so that the models themselves could be analyzed separately, but the function definitions only needed to be modified once within the library whenever an error was detected. A documentation of this library is provided in Appendix C.

Within each analysis file, once the simulation data is loaded and the data cuts made according to Figure 2, I identified satellite systems by their host. For each host, the positions of the bound subhalos give the spatial distribution of the system, and the stellar mass within each subhalo indicates the luminosity of the subhalos: the more massive the subhalo, the more luminous it is. I require only the ten most luminous subhalos in each satellite system, excluding the central subhalo, and so I only select hosts that have more than ten subhalos around them to start. For the assessment of the plane kinematics, the relative velocities of these subhalos are also returned, which aids in further computing the specific angular momenta (Equation 4) and relevant quantities.

I would like to fit a plane through these ten luminous subhalos, and so it is important to ensure that their positions are handled carefully. With information about the position of the central subhalo (the host) and the size of the periodic box used in the simulation, I get a set of subhalo coordinates (and relative velocities) that are centered around the host and corrected (in the case of positions) for the periodic boundary (Equation 1). The arithmetic mean of these points yields the position of the centroid relative to the host (Equation 2). In a classic shifting-the-origin problem, the host-centered coordinates are now centered around the centroid (Equation 5). Thus, there are now two distributions to work with: the centroid-centered distribution and the host-centered distribution.

To both these distributions, the function INERTIA_TENSOR() is applied, yielding the normal to the thinnest plane fit. In addition, the axis ratios (relative plane flattening) and plane thickness are also recorded. Using the coordinates of the center of the reference frame — host and centroid — the missing variable D is calculated (Equation 7), forming two full sets of plane coefficients: one plane in the host-centered frame, and one in the centroid-centered frame.

The two sets of plane coefficients are further used to calculate plane thicknesses and the angle between the two planes. The RMS radial extent is also calculated and recorded. The plane thicknesses measured by the INERTIA_TENSOR() function and those measured using the plane coefficients are one-to-one and can be used interchangeably.

In addition to the centroid offset d calculated in Equation 2, we define an additional quantity $d_\perp$, which is the *plane offset*. Given the position of the host halo in the centroid-centered frame (which is the position of the centroid with the signs reversed) and the plane coefficients of the plane passed through the centroid (Equation 7, 11), this is the perpendicular distance from the point to the plane.

$$\begin{aligned} \mathbf{r}_{\text{host, cc}} &= -\mathbf{c} \\ d_\perp &= \frac{|(\mathbf{n_c} \cdot \mathbf{r}_{\text{host, cc}}) - D|}{|\mathbf{n_c}|} \end{aligned} \tag{15}$$

Having defined the specific angular momentum and orbital pole in Equation 4, and the plane normal in Equation 11, a few further kinematic features of the plane can be assessed, namely, the RMS angle between the orbital poles of the subhalos and the plane normal; and the orbital pole dispersion, which is the scatter of the individual poles away from the mean orbital pole. These two values are summarized in Table 1 and Equation 16. Equation 16 is used for the host frame.

$$\begin{aligned} \theta_{rms} &= \langle [\arccos{(\hat{h} \cdot \hat{\mathbf{n}})}]^2 \rangle \\ \bar{\theta} &= \langle \hat{h} \rangle \\ \theta_i &= \arccos{(\hat{h} \cdot \bar{\theta})} \\ \Delta_{sph} &= \sqrt{\frac{1}{k} \sum_{i=1}^{k} \theta_i^2} \end{aligned} \tag{16}$$

The equation for Δ_{sph} is used from [2] and indicates the RMS scatter of all orbital poles around the k most concentrated poles. Since $k = 10$ makes a full set, that is the default value used in the calculations, and $\Delta_{sph}(k)$ in [2] is simply Δ_{sph} in this work. A θ_{rms} of 90° would therefore indicate that there is *no kinematic coherence* between the fit plane and the relative velocities, while values closer to 0° or 180° would indicate a strong kinematic coherence. In order to assess the 0° and 180° cases separately, θ_{rms} is calculated twice: once using the plane normal as it is, and once using $-\hat{\mathbf{n}}$. The lower value of θ_{rms} computed this way is reported to the main pipeline and subsequent values then choose the direction of $\hat{\mathbf{n}}$ — positive or negative — to measure the other values described in Equation 16.

The host-centered satellite distributions, along with the fit planes, are saved as an interactive HTML file, along with Mollweide projections of the angular momenta of the satellites, and their apparent positions and velocities. The full set of outputs from the algorithm is summarized in Appendix B, and a sample output is shown in Appendix C.

3.4 The Isotropic Case

With the radial and velocity distribution data readily available, another assessment to be made is to compare the dark matter models to the case where the position and velocity vectors are completely randomized. To do so, samples of the radial and velocity distributions — the magnitudes of the respective vectors for position and relative velocity — are fed to a function that takes the magnitudes and randomizes the directions they point towards. A spherical coordinate system is used for this.

$$\begin{aligned}
x &= r\sin\theta\cos\phi \\
y &= r\sin\theta\sin\phi \\
z &= r\cos\theta \\
\\
v_x &= v\sin\theta\cos\phi \\
v_y &= v\sin\theta\sin\phi \\
v_z &= v\cos\theta
\end{aligned} \tag{17}$$

Here, r and v are chosen from a sample of radial distributions or velocity distributions, respectively. A sample of the radial distributions and all the velocity distributions for each satellite system and for each model is predefined. The angles θ and ϕ are randomized separately for position and velocity vectors.

The idea then is to choose one set of radial distributions from the radial distributions sample, and the corresponding set of velocities from the velocity distribution sample. I assume one-to-one correspondence between the two sets: the first value in the set of chosen r has the first value of the velocity v in the chosen velocity set. These values are made to "point" in a randomized distribution according to Equation 17. Similar to the procedure outlined in Section 3.3, these datasets are now evaluated based on their best-fit plane and kinematics. The values compared are c/a, b/a, R, Δ_{rms}, θ_{rms}, and Δ_{sph}. They are plotted with the dark matter models in Section 4, where the significance of their overlaps is also discussed in terms of statistical tests.

One thousand runs were conducted for the isotropic case. A full algorithm for this procedure is outlined in Appendix A.

4 Results

Using the group number field as a primary key allows for cross-matching when loading an additional dataset for analysis: the masses of the host halos. Doing so allows us to evaluate the number of satellites per halo against the mass of the halo, and compare other plane properties similarly.

4.1 Central Tendencies in Data

The final N_{sat} are compared to each other by model in Figure 8. In addition to the host masses and the individual satellite counts plotted against host masses (Figure 10a, 10b, 10c, 10d), this plot shows that there is no bias in the way hosts and subhalos are chosen for analysis. This is further confirmed in Section 4.2 (Table 3). I interpret the apparent "rise" of the fraction of WDM3 satellite systems (green) compared to CDM (blue) or vSIDM (orange) to show that at 80% on the y-axis, the WDM3 curve is more shifted to the left: towards the *fewer* number of satellites per host. The WDM3 curve rises earlier — making up a greater fraction of the full sample of hosts at a smaller N_{sat} — where the CDM and vSIDM models stay well under it. That is to say, *a larger fraction of hosts in the WDM3 model have fewer luminous satellites than CDM or vSIDM.* This is an expected result following [50], given that WDM3 was formulated in part to solve the missing satellites problem, and therefore suppresses the formation of low-mass subhalos.

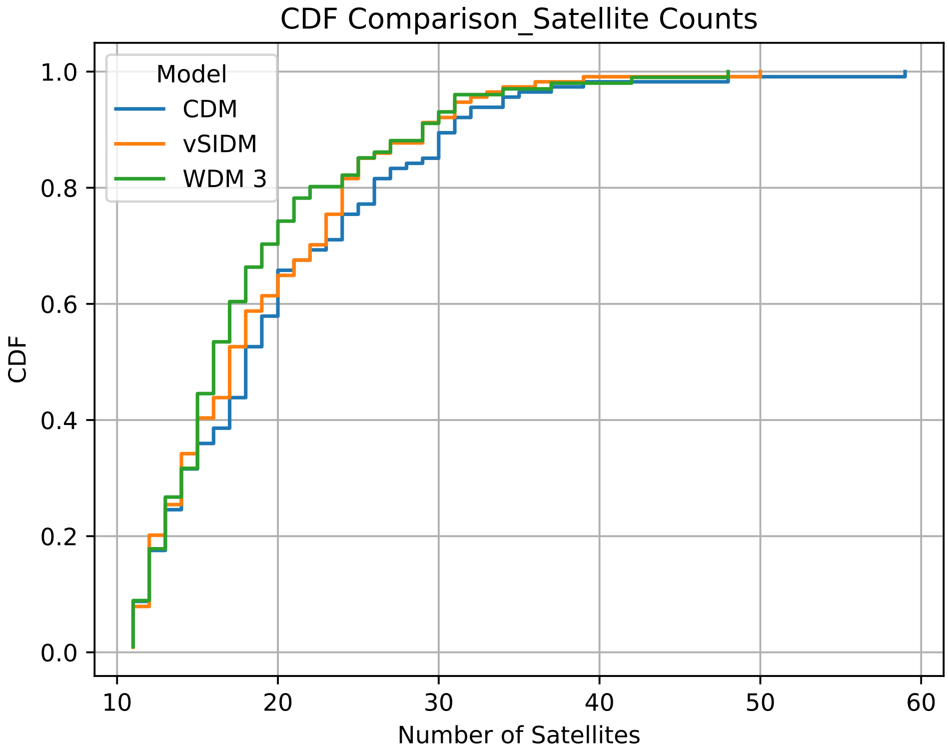

Figure 8: Comparison of CDFs of N_{sat} per model. Despite the apparent shift between WDM3 (green) and CDM (blue), the K-S tests (Table 3) indicate no significant effect of the dark matter model on the number of satellites per host.

While these satellite counts encompass *all* the luminous subhalos that fulfill the criteria set out in Figure 2, the plane fitting is only applied to the ten most luminous satellites, besides the central subhalo, of a system. The radial distributions and relative velocities of these systems, accounting only for the top 10 luminous subhalos, are outlined in Figure 9. In these figures, there are a few systems that extend beyond 1000 kpc (1 Mpc) from the host. WDM3 systems appear to be more radially extended, and CDM the least so. There is relatively little scatter to be found in the velocity distributions, by comparison. The distributions in Figure 9 also show the median for each model, the 25$^{\text{th}}$ and 75$^{\text{th}}$ quartiles, and a shaded region between the median and the quartiles.

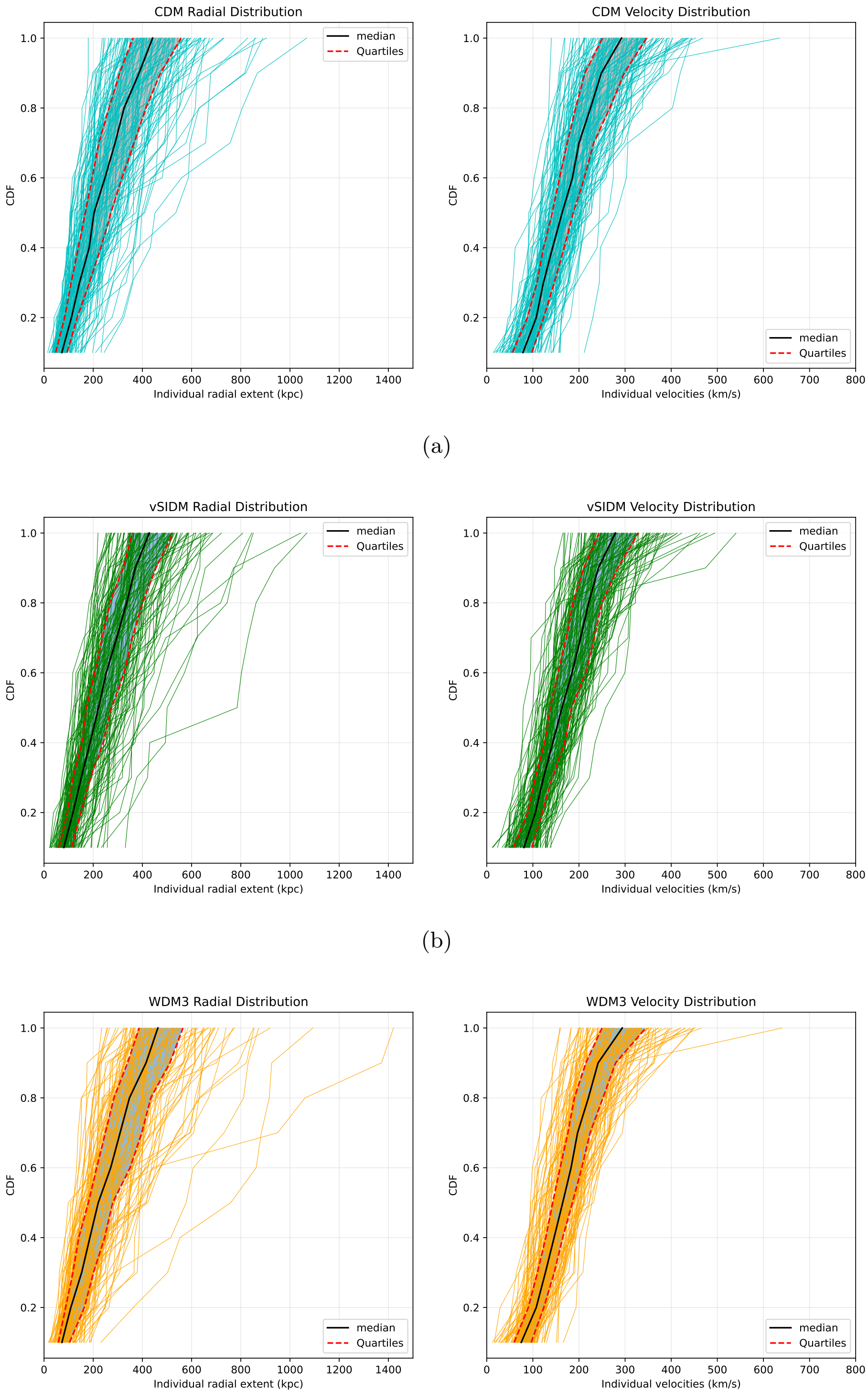

(a)

(b)

(c)

Figure 9: The radial and velocity distributions for (a) CDM, (b) vSIDM, and (c) WDM3. All models show at least one extended system, identifiable in the code. Velocities appear more tightly packed. The median radial extent (or velocity) and a range between ±50% of the median is shaded in all figures.

Comparing Figure 10b, 10c, and 10d, there seems to be no difference between the distributions of the host masses and N_{sat} among the three models. This fact is further demonstrated numerically when the cumulative distribution functions (CDFs) for the two values are plotted (Figure 2, Table 2, Figure 8, Figure 10a). Looking at the steady rise in the cumulative distributions in Figure 10a, there appear to be nearly an equal number of hosts in each mass interval. Statistical tests confirm that the host masses can be reasonably interpreted to be drawn from the same sample. This also simplifies the analysis of plane fitting and kinematic results: we may safely rule out any effect of the host halo mass on the plane properties.

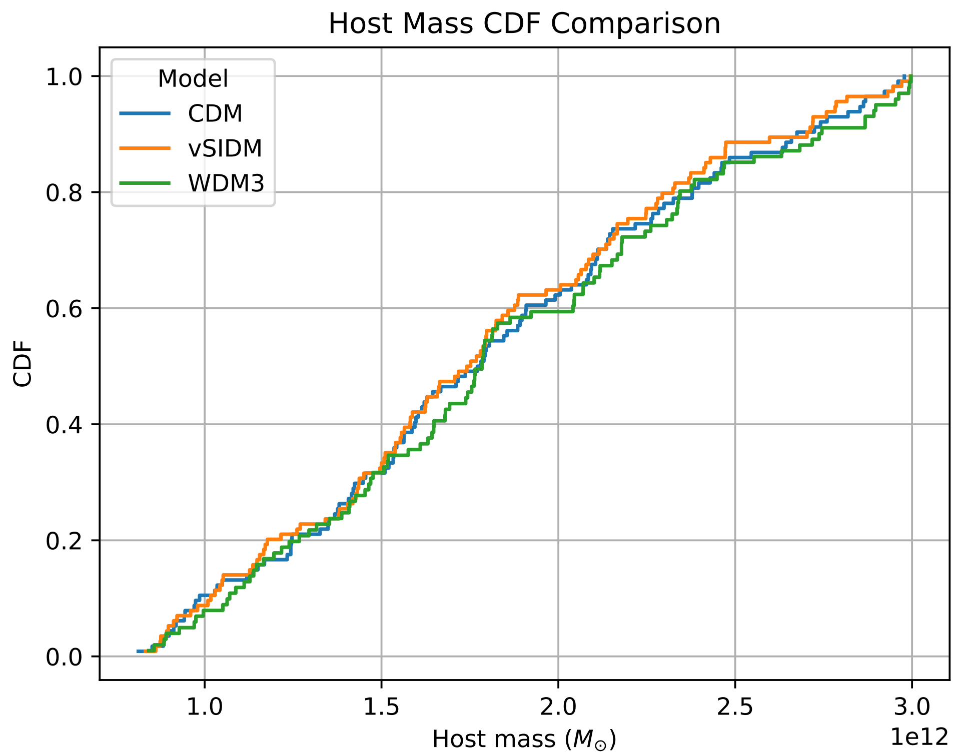

(a)

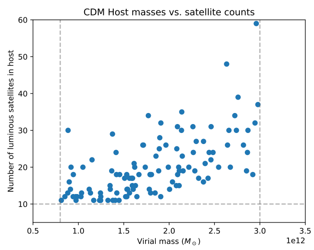

(b)

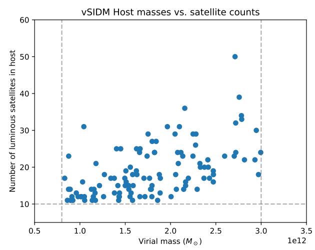

(c)

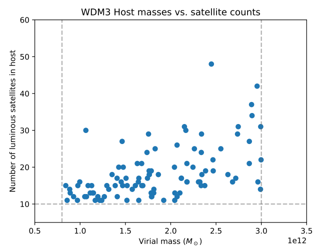

(d)

Figure 10: (a) Cumulative distribution of host masses M_{200} across models. The unit on the horizontal axis is solar masses ($M_\odot$). The overlap of the models shows that the mass distribution will not skew further analysis. (b) Number of luminous satellites (y-axis) against host mass ($M_\odot$, x-axis) in CDM. (c) Number of luminous satellites (y-axis) against host mass in vSIDM. (d) Number of luminous satellites (y-axis) against host mass ($M_\odot$, x-axis) in WDM3. In (b), (c), and (d), the vertical lines indicate the lower and upper limits on M_{200}. The horizontal line indicates the threshold for N_{sat} at 10.

Quantity	CDM	vSIDM	WDM3
Median M_{200} ($M_\odot$)	1.78×10^{12}	1.75×10^{12}	1.78×10^{12}
Median d (kpc)	99.36	100.65	112.72
Median $d_\perp$ (kpc)	34.05	35.49	33.79
Median c/a ratio	0.382	0.401	0.391
Median b/a ratio	0.649	0.657	0.665
Median Δ_{rms} (kpc)	83.38	88.35	88.04
Median R (kpc)	283.247	283.018	303.690
Median Δ_{sph} (deg)	76.39	76.66	76.00
Median θ_{rms} (deg)	89.66	88.99	88.77

Table 2: Medians of the properties analyzed for each model, showing little to no effect of the dark matter model on host mass selection.

Table 2 lists out all the median values measured in this work for all three dark matter models. The individual results are discussed at length in the upcoming sections, but I have an initial assessment: these values are nearly in agreement with each other. Even so, we may look at individual quantities such as the relative flattening or the c/a ratio, which seems to have the lowest median in CDM. Further, the absolute flattening of the planes, quantified by Δ_{rms}, also has the lowest median for CDM. On the other hand, the median radial extent and centroid offset are the largest for WDM3. A larger R is an expected result, further discussed in Section 4.2. Based on these results alone, if one had to name a model at all, it would seem that CDM produces the flattest planes. If anything, changing the dark matter model may *reduce* the occurrence of satellite planes.

For the kinematics portion, the angular values do not improve the impression. θ_{rms}, the RMS alignment between the plane normal and the orbital poles, has a median value of nearly 90°, suggesting that there is no kinematic coherence in the fit satellite planes. The orbital pole dispersion medians are also nearly equal between models, and show no kinematic coherence that suggests that the satellites move in a plane, or that they move in the best-fit plane for the spatial distribution. In the upcoming subsections, these results are discussed in the context of statistical tests.

4.2 K-S Tests: Comparisons Between Models (Spatial Distribution)

In order to evaluate the CDFs presented in Figure 8, Figure 11, Figure 10a, and Figure 12, I employ the Kolmogorov-Smirnov (K-S) test. This test is used to compare either a theoretical distribution to empirical data in the form of a cumulative distribution function, or two empirical data curves presented as cumulative distribution functions. Of the two, the latter is more relevant to the present analysis.

Of importance is the null hypothesis given for the two-sample K-S test: *the two curves are sampled from the same distribution.* In the context of the present work, there are three cumulative distribution curves for a given property of the satellite system, of which two will be compared at a time. Each of these curves represents a theoretical model of dark matter. When we make a comparison of the cumulative distributions, therefore, we are asking the question, *how does the underlying dark matter model affect the shape of the curve?* Here, the null hypothesis can then be formulated as, *the underlying model of dark matter does not affect the shape of the distribution.*

The values measured by the K-S test are D and p. D is the maximum separation between the two cumulative distributions being assessed. The value p, reported as the p-value, measures the likelihood of obtaining the value D, given the sample sizes of the two distributions, if they were indeed drawn from the same sample. If the two distributions indicate the same sample, then the null hypothesis is confirmed, and a high p-value is reported. For a value $p < 0.05$, the null hypothesis is rejected. In this case, one admits the possibility that the two distributions *do not* come from the same sample, implying that the dark matter model affects the property being assessed.

Tables 3, 4, and 5 summarize the K-S test results for several data metrics. Since the test measures the maximum separation of the cumulative distribution functions, the computational implementation of the K-S parameter also indicates the model with the greater fraction value (i.e., higher up on the CDF in its corresponding plot).

Parameter	**Comparison Models**	D	$p-$value
M_{200} $(M_\odot)$	**CDM, vSIDM**	0.053	0.998
	CDM, WDM3	0.081	0.835
	WDM3, vSIDM	0.081	0.835
N_{sat}	**CDM, vSIDM**	0.088	0.775
	CDM, WDM3	0.165	0.092
	vSIDM, WDM3	0.107	0.529

Table 3: K-S Test results for M_{200} and N_{sat}. It is to be noted that none of the $p-$values is under 0.05, at which point the null hypothesis - that there is *no* effect of the dark matter model on the result - could have been rejected.

Of interest are also the centroid offset d and the plane offset $d_\perp$. All three models show systems where the value of d is above 300 kpc. One system in vSIDM also has $d_\perp > 250$ kpc, which may have increased the median value in the vSIDM model (Table 2). However, there is again no effect of the dark matter model on the centroid offset or plane offset to be found, as all $p-$values are above 0.05 (Table 4). For the present sample, all values are statistically consistent with each other, showing no effect of the dark matter model on these quantities.

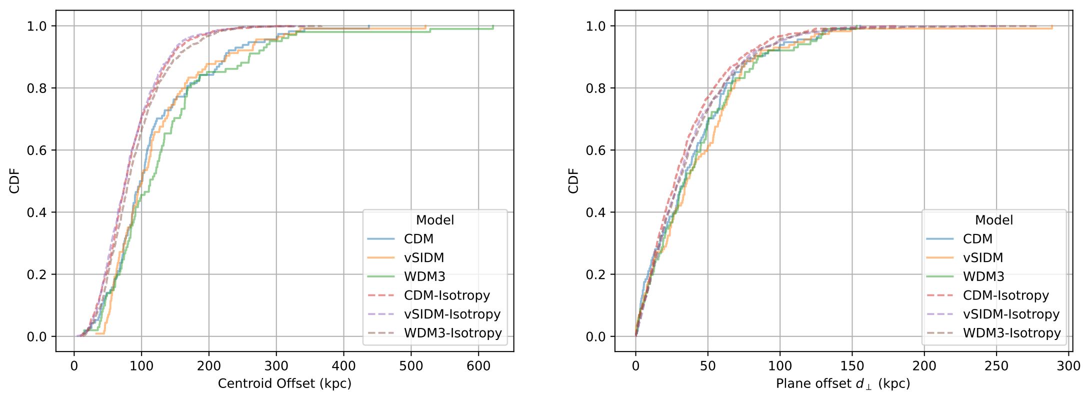

Figure 11: Left: Comparison of centroid offset across models. Right: Comparison of plane offset across models. Both properties are compared with the isotropic cases of the three dark matter models, shown here in dotted lines.

Parameter	Comparison Models	D	p-value
d (kpc)	CDM, vSIDM	0.105	0.555
	CDM, WDM3	0.168	0.083
	vSIDM, WDM3	0.134	0.258
	CDM-Isotropic	0.230	0.00003
	vSIDM-Isotropic	0.240	0.00001
	WDM3-Isotropic	0.272	0.000002
$d_\perp$ (kpc)	CDM, vSIDM	0.097	0.666
	CDM, WDM3	0.067	0.953
	vSIDM, WDM3	0.099	0.610
	CDM-Isotropic	0.112	0.139
	vSIDM-Isotropic	0.136	0.040
	WDM3-Isotropic	0.096	0.338

Table 4: Statistical tests for the centroid and plane offsets. They are compared once amongst themselves, and then each dark matter model is compared with its respective isotropic case.

It is interesting to note the deviation of the centroid offsets in the dark matter simulations against their equivalent isotropic runs, and the deviation of the plane offset from its isotropic case in vSIDM in Table 4. For the centroid offset, it may be understood as the fact that when we use the radial distributions from the dark matter models, but scatter them randomly in a spherical distribution, we effectively decrease the mean of the radial distribution. For example, there may be systems in the isotropic case where the closest and farthest points happen to lie on a straight line passing through the origin, but on diametrically opposing sides. There may also be cases where all points happen to be in only one or two octants of the three-dimensional space, in which case there are higher centroid offsets recorded. The isotropic distribution differs from the dark matter simulations in an important way: *they do not account for the mechanisms by which these satellites were bound to the host.*

The extreme cases of the extended CDFs for d and $d_\perp$ are accounted for by the fact that the isotropic run covers 1000 cases. There are systems in the isotropic case, as in the dark matter simulations, where the centroid offset is greater than 300 kpc; there is also a system in the isotropic case where the plane offset is greater than 250 kpc, although not in the same dark matter model (the simulations show it for vSIDM, but the isotropic case shows a WDM3 system in Figure 11). This may be an effect of the radial distributions, as from Figure 9, we see that both vSIDM and WDM3 have more radially extended systems than CDM. Further, the dark matter models also show greater "lopsidedness" (especially as measured by higher centroid offsets) because they account for the evolution history of the host-satellite system, where group infall and movement along filaments affect these structures, as explained in Section 1.3.1.

To compare the occurrence of planes in the various dark matter models and compare them to each other and their isotropic cases, the plane properties under assessment were the c/a ratio, the b/a ratio, Δ_{rms}, and R, all in the host-centered frame. The results from Figure 12 are what aid in answering the research question posed in Section 1.5.

Figure 12 shows the plane properties defined by the spatial distribution of the satellites. These are the relative flattening of the plane along the minor and intermediate axes (the c/a ratio and the b/a ratio, respectively, on the top row), the absolute flattening of the plane (the RMS heights, or Δ_{rms}, bottom left), and the RMS radial extent of the fit plane R (bottom right). The cumulative distributions of the dark matter models are plotted along with the same data, but with randomized vectors for the isotropic case, as discussed in Section 3.4.

A first impression of the plots shows a large overlap in the dark matter models among themselves, and also in the isotropic distributions. However, there appears to be a separation between the dark matter models and their respective isotropic cases. Whether this separation is statistically significant is summarized in Table 5.

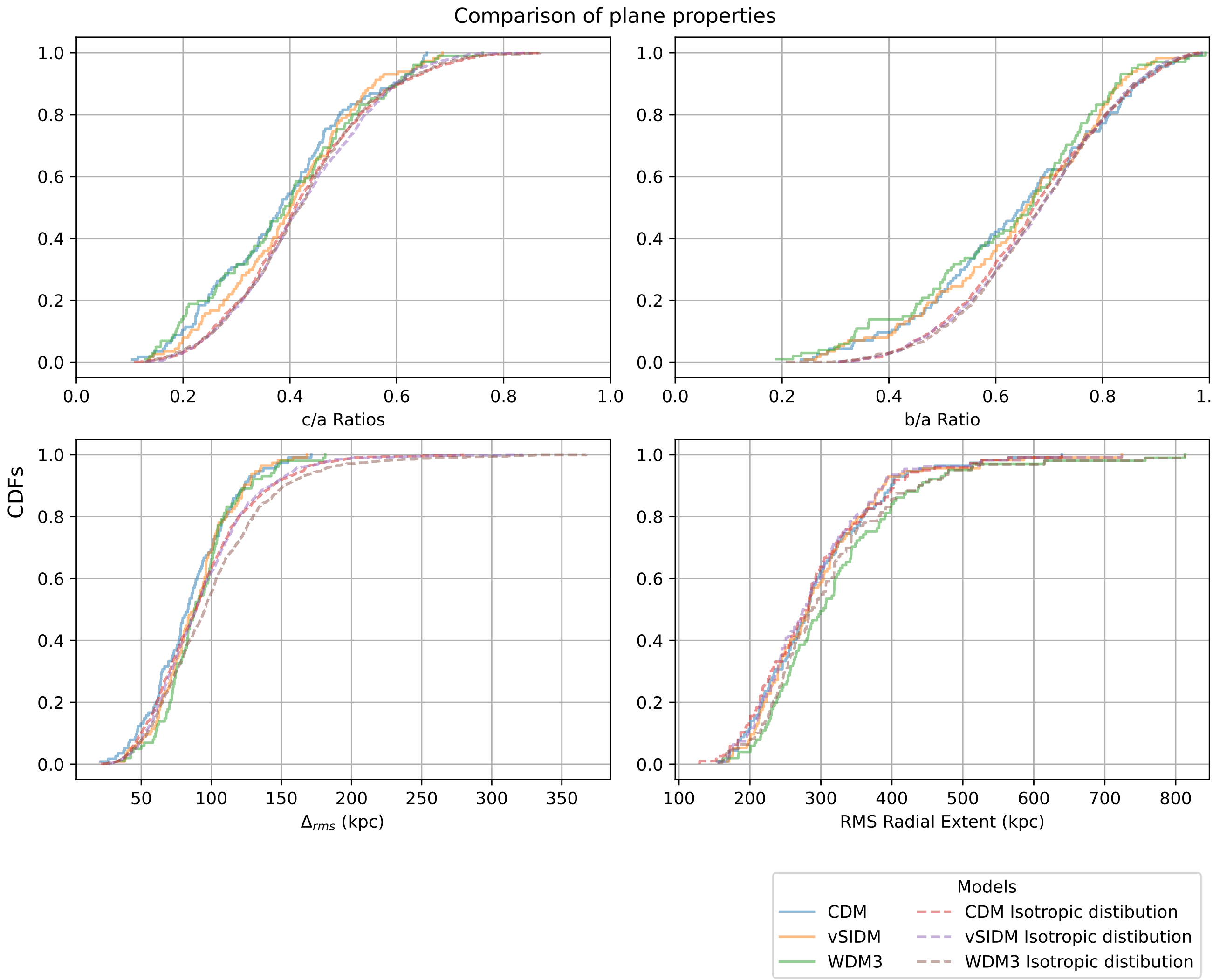

Figure 12: Plane properties of all models in the host-centered frame. Dotted lines indicate the assessment of the simulation data when distributed in an isotropic manner.

Quantity	Models compared	K-S Parameter	$p-$value
c/a Ratio	CDM, vSIDM	0.097	0.666
	CDM, WDM3	0.074	0.901
	vSIDM, WDM3	0.100	0.605
	CDM, Isotropic case	0.148	0.020
	vSIDM, Isotropic case	0.091	0.344
	WDM3, Isotropic case	0.146	0.036
b/a ratio	CDM, vSIDM	0.088	0.775
	CDM, WDM3	0.094	0.684
	vSIDM, WDM3	0.081	0.834
	CDM, Isotropic case	0.145	0.024
	vSIDM, Isotropic case	0.124	0.078
	WDM3, Isotropic case	0.176	0.006
Δ_{rms} (kpc)	CDM, vSIDM	0.097	0.666
	CDM, WDM3	0.177	0.059
	vSIDM, WDM3	0.089	0.739
	CDM, Isotropic case	0.086	0.415
	vSIDM, Isotropic case	0.114	0.130
	WDM3, Isotropic case	0.163	0.014
R (kpc)	CDM, vSIDM	0.053	0.998
	CDM, WDM3	0.144	0.190
	vSIDM, WDM3	0.148	0.166
	CDM, Isotropic case	0.044	0.983
	vSIDM, Isotropic case	0.045	0.979
	WDM3, Isotropic case	0.077	0.614

Table 5: Test statistics for plane properties as shown in Figure 12.

There is no p-value in Table 5 that is under 0.05 when comparing the dark matter models among themselves, though Δ_{rms} between CDM and WDM3 sits at the edge of significance. Even so, looking at the median value of Δ_{rms} for the two values (Table 2), it appears that the flatter planes are produced in CDM, if any one model has to be named at all. Comparing this result with the radial distribution plots (Figure 9), however, this appears to be an effect of the fact that WDM3 models are more extended than the CDM ones. Although I have only compared three models and there is scope for more models, there is *no indication* within this data that plane properties are strongly dependent on the adopted dark matter model.

However, a few models show a significant deviation from the isotropic case ($p < 0.05$). It is especially notable for the c/a and b/a values of CDM and WDM3 and the value of Δ_{rms} for WDM3. In all cases, it appears that the dark matter models favor flatter planes, as seen in Figure 12. The isotropic cases push the value of Δ_{rms} to 350 kpc: the systems where this occurs may have been so randomized that they resembled a sphere more than a plane. The lack of significance in the dark matter models and their isotropic cases for R is attributed to the fact that I did not change the radial distributions themselves, but rather drew from the simulation data. Essentially, the radial distributions for the dark matter case and the isotropic case were indeed drawn from the same sample.

In this analysis, I equalized the number of satellites for each host at ten luminous subhalos per host. I also did not set limits, or "thresholds," to define what can be identified as a plane and what cannot. Both of these choices minimize bias in reporting these results. A smaller number of points considered would increase the likelihood of thinner planes, for example — three points always lie on a plane — and determining arbitrary thresholds deliberately reduces the size of what is already a fairly small sample (Figure 2). In this way, the sampling bias is minimized.

4.3 K-S Tests: Comparisons Between Models (Kinematics)

The results from two measurements of plane kinematics are presented in this section: θ_{rms}, or the RMS angle between the orbital poles and the plane normal, and Δ_{sph}, the orbital pole dispersion as the angle between the mean orbital pole and individual orbital poles.

In Figure 13, the cumulative distributions of θ_{rms} are shown for all three dark matter models and their isotropic cases. There is again an overlap between the dark matter models, and a slight separation between them and their isotropic cases. The idea here is to measure how well the plane normal aligns with the orbital poles: if the two vectors are parallel (or anti-parallel), the RMS angle must be 0° (or 180°), and the satellites orbit in a plane, specifically in the best-fit plane. On the other hand, if this value is closer to 90°, then neither is there any kinematic coherence to be found, nor do the satellites orbit in the best-fit plane.

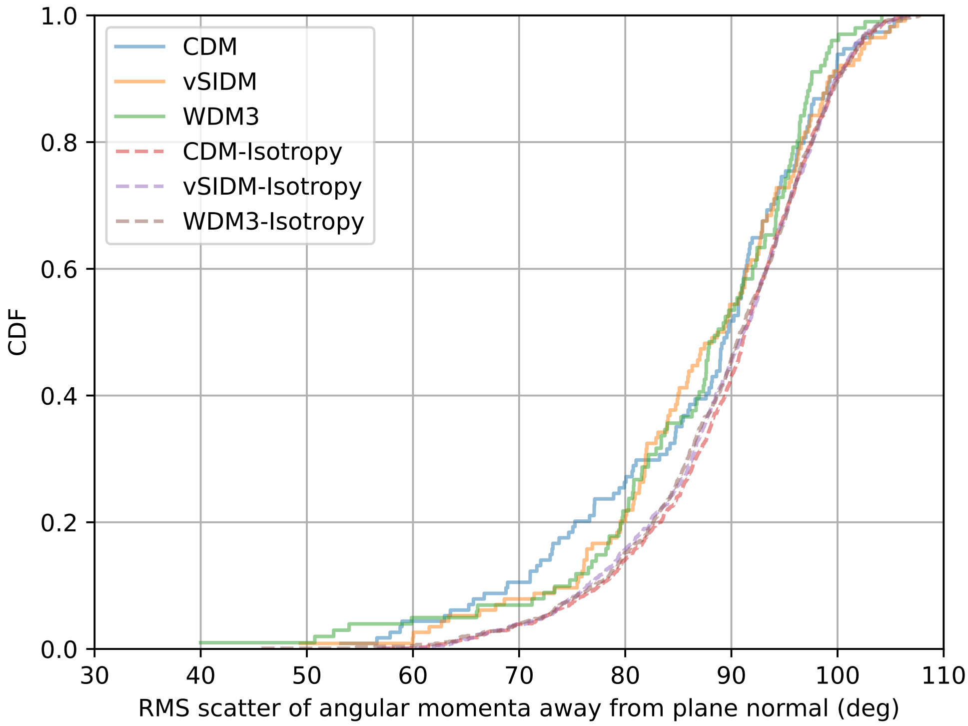

Figure 13: The cumulative distributions of θ_{rms} for all three dark matter models (solid lines), compared to their respective isotropic cases (dashed lines).

In Table 6, the K-S tests for θ_{rms} (and Δ_{sph}) are summarized. For the θ_{rms} values, we see that there is again no significant effect of the model on kinematic coherence. There is also no kinematic coherence to be found, as in Figure 13, most values fall between 60° and 100°. The same can be said for the isotropic cases, which show even greater angular values. This is understandable because the isotropic case is always the case with the highest degree of randomness. Dark matter, regardless of the model, introduces a small but significant kinematic coherence into these systems. This is also supported by $p < 0.05$ in the case of CDM and vSIDM against their isotropic cases. There is no significant deviation from isotropy in the case of WDM3.

Figure 14 shows the cumulative distribution for the orbital pole dispersion Δ_{sph}. This value is the statistical dispersion of the individual orbital poles versus the mean orbital pole, quantifying whether all orbital poles point more or less in the same direction. Once again, values closer to 0° or 180° show greater clustering of orbital poles, while a value closer to 90° shows that the orbital poles are more scattered. In the figure, we see most values between 60° and 100°, indicating no clear pattern of clustering.

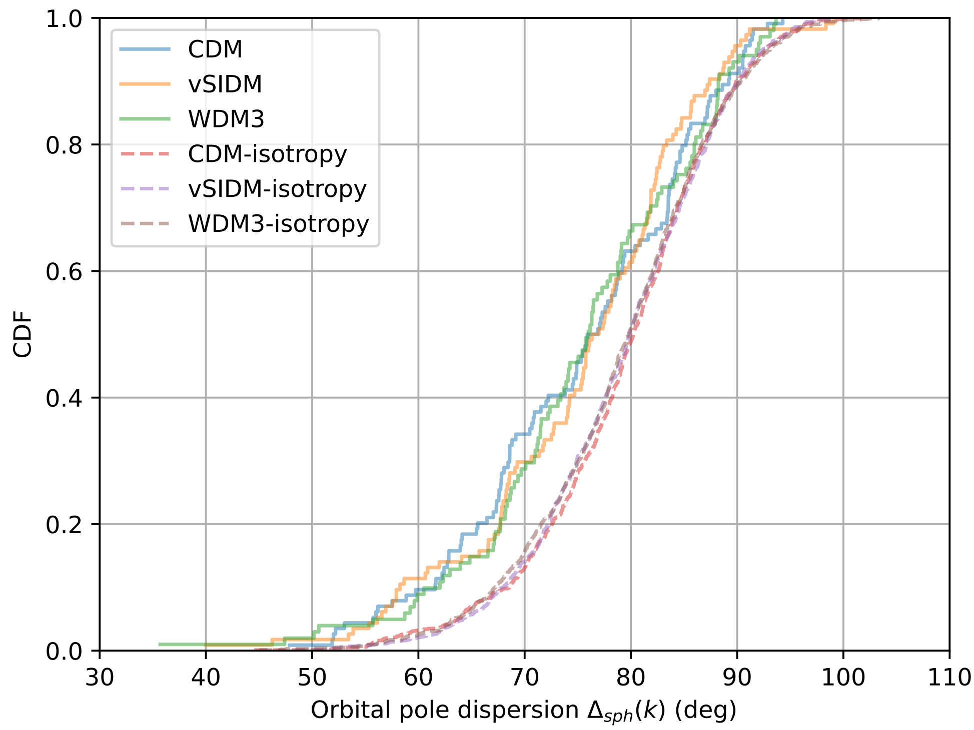

Figure 14: The cumulative distributions of Δ_{sph}, defined in [2], for the dark matter models (solid lines) and their isotropic cases (dashed lines).

Quantity	Models Compared	K-S Parameter	p-value
θ_{rms} (deg)	CDM, vSIDM	0.105	0.555
	CDM, WDM3	0.098	0.632
	vSIDM, WDM3	0.072	0.915
	CDM, Isotropic case	0.143	0.027
	vSIDM, Isotropic case	0.152	0.015
	WDM3, Isotropic case	0.121	0.122
Δ_{sph} (deg)	CDM, vSIDM	0.132	0.278
	CDM, WDM3	0.087	0.769
	vSIDM, WDM3	0.096	0.657
	CDM, Isotropic case	0.228	0.00004
	vSIDM, Isotropic case	0.170	0.005
	WDM3, Isotropic case	0.206	0.0007

Table 6: K-S test results for all models and their isotropic cases from Figures 13 and 14.

In Table 6, looking at the Δ_{sph} results specifically, not only do we find a lack of orbital pole clustering, but also no effect of dark matter model on the degree of clustering. However, I note that the p-value for the dark matter models against their isotropic cases is significant for *all three* models. Randomizing the directions of the position and velocity vectors makes the satellite systems *more* incoherent, pushing the distributions towards *lesser* clustering. Similarly to the case of θ_{rms}, dark matter, regardless of the model, introduces a small but significant amount of kinematic coherence.

4.4 Plane Properties by Host Masses

The following figures weigh each plane property, shown in Figure 12 and Table 5, against the host mass, while the color of each plot point shows N_{sat} for the system.

I operate on the null hypothesis that there is *no correlation* to be found between plane properties and host masses. A $p-$value < 0.05 rejects this null hypothesis (and therefore indicates a correlation), and $p > 0.05$ confirms the null hypothesis.

The tests being conducted are Pearson's r (test for linear correlation), Spearman's ρ (testing any general monotonic relation), and Kendall's τ (assessment of direct or inverse proportions in the data).

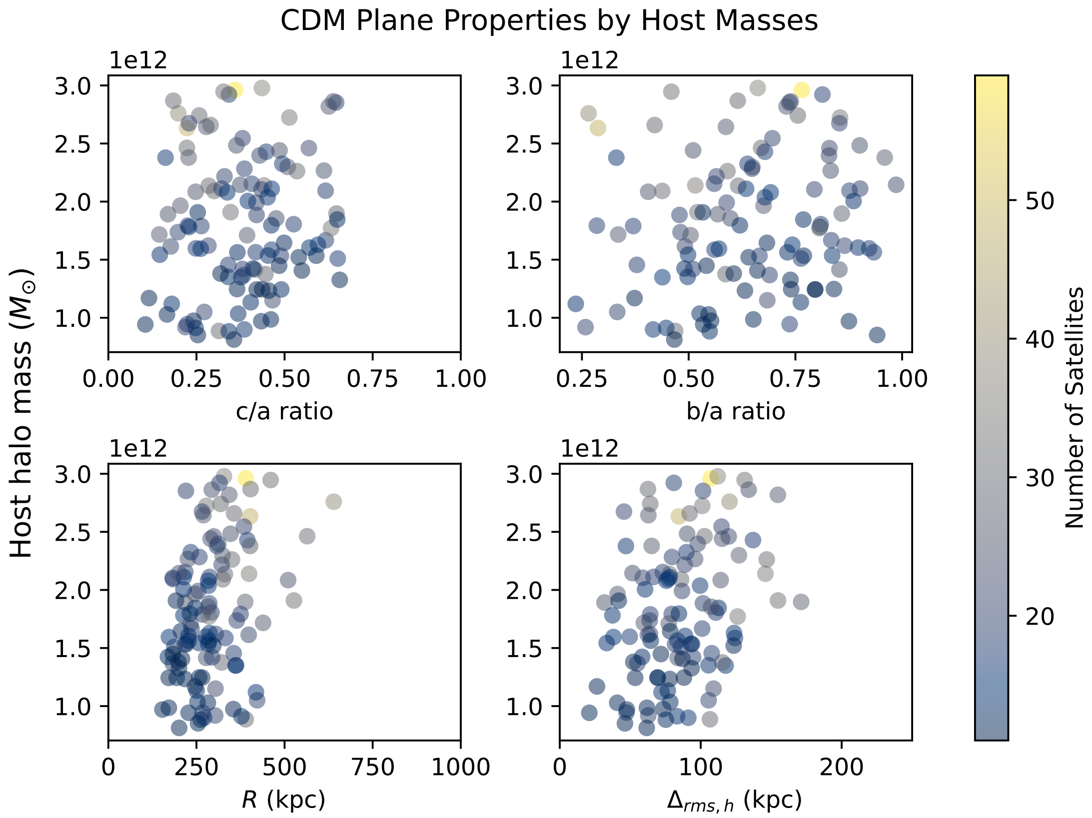

Figure 15: For CDM, the four metrics evaluating plane properties and any possible correlation between the respective property and host mass. Data points are colored on the basis of N_{sat} as referenced by the color bar on the right of the image.

If there is any correlation to be found at all, it is extremely scattered. The results are summarized in Table 7 for CDM.

Test	Plane Property (against M_{200})	Statistic	$p-$value
Pearson r	c/a ratio	0.105	0.266
	b/a ratio	0.148	0.116
	R	0.328	0.0004
	Δ_{rms}	0.328	0.0004
Kendall τ	c/a ratio	0.062	0.331
	b/a ratio	0.113	0.074
	R	0.223	0.0004
	Δ_{rms}	0.213	0.0007
Spearman ρ	c/a ratio	0.084	0.375
	b/a ratio	0.163	0.083
	R	0.321	0.0005
	Δ_{rms}	0.312	0.0007

Table 7: Correlation statistics for CDM plane properties

From Table 7, I conclude that there is no correlation between the host masses and the axis ratios (which measure the relative flattening). There is, however, a positive correlation to be found for R and Δ_{rms}: in other words, between the host mass and the absolute measure of flattening, and between the host mass and the radial extent of the system. This is to be expected, as more massive hosts have more radially extended systems [69]. The correlation is very loose, however, based on the scatter in the plots, and reflected in the near-equal values for Pearson's r and Spearman's ρ coefficients. A case could be made for a positive linear correlation with scatter. This is supported by [70] and [71], both finding linear fits for observational and simulation data.

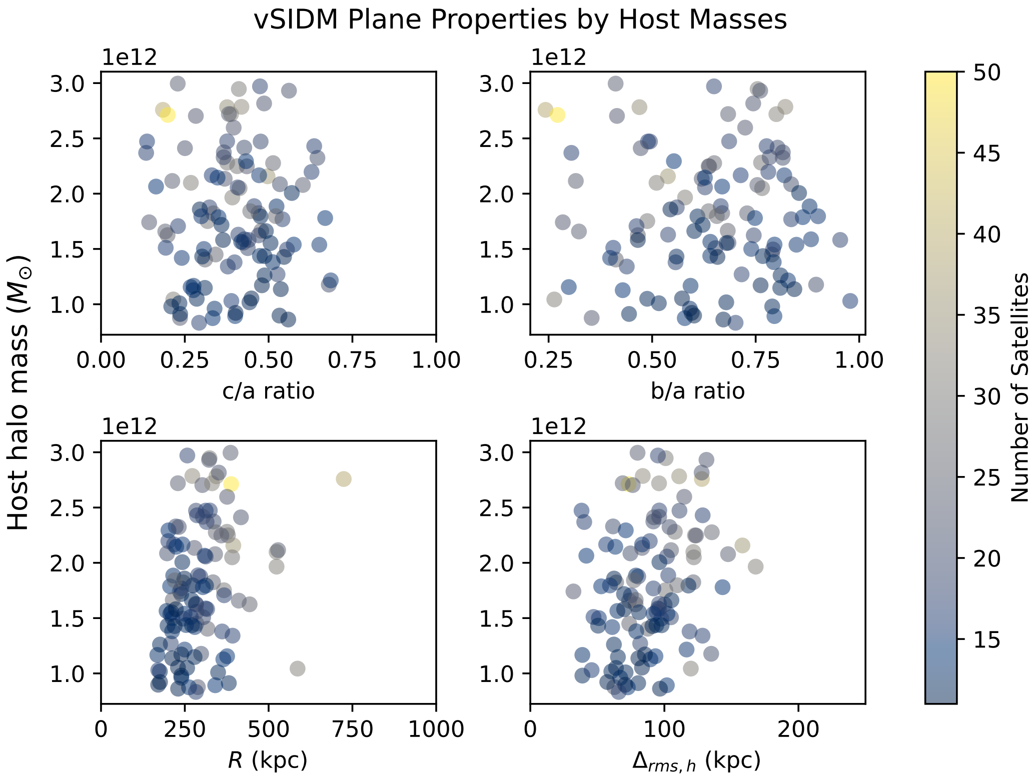

Figure 16: For vSIDM, the four metrics evaluating plane properties and any possible correlation between the respective property and host mass. Data points are colored on the basis of N_{sat} as referenced by the color bar on the right of the image.

In Figure 16, showing the comparisons of the plane properties against host masses, similarly to Figure 15, we may expect to find more significant linear correlations in R and Δ_{rms}. The c/a ratio visually shows more clustering of data points, but that is simply due to the axis scaling of the plot, which is uniform across all three models (Figures 15, 16, 17). Statistically, there is a slight difference in the reported numbers, as shown in Table 8.

Test	Plane Property (against M_{200})	Statistic	$p-$value
Pearson r	c/a ratio	-0.0004	0.997
	b/a ratio	-0.013	0.888
	R	0.287	0.002
	Δ_{rms}	0.272	0.003
Kendall τ	c/a ratio	0.010	0.874
	b/a ratio	0.010	0.870
	R	0.212	0.0008
	Δ_{rms}	0.194	0.002
Spearman ρ	c/a ratio	0.016	0.866
	b/a ratio	0.023	0.804
	R	0.310	0.0008
	Δ_{rms}	0.285	0.002

Table 8: Correlation statistics for vSIDM plane properties

The vSIDM model shows no correlation between axis ratios and host masses. Further comparing the Pearson and Spearman statistics, one again finds a correlation between host masses and R and Δ_{rms} with near-equality in the two coefficients, indicating a positive linear correlation. The Kendall statistic confirms the positive correlation. I therefore conclude that there is a linearly increasing correlation with large scatter.

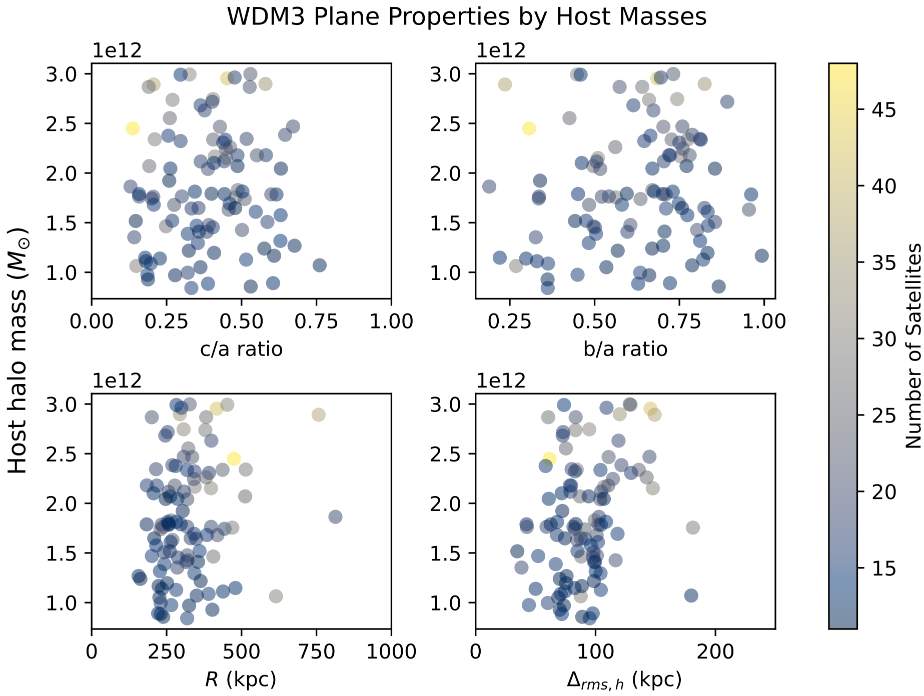

Figure 17: For WDM3, the four metrics evaluating plane properties and any possible correlation between the respective property and host mass. Data points are colored on the basis of N_{sat} as referenced by the color bar on the right of the image.

Figure 17, especially in the first two panels showing the relative flattening of the planes, shows a larger scatter than Figures 15 and 16. In the two lower panels of the image, indicating absolute plane thicknesses and the radial extents of the planes, even though there appears to be a correlation with a scatter, the outliers appear to be starker than in the previous two models. For example, while most of the data points for R are within $\sim 500\,\mathrm{kpc}$, three outliers are seen in the panel at distances beyond $600\,\mathrm{kpc}$ with no points in between. To our advantage, the correlation tests (with the exception of Pearson r) are not sensitive to these outliers.

Test	Plane Property (against M_{200})	Statistic	$p-$value
Pearson r	c/a ratio	0.058	0.568
	b/a ratio	0.118	0.242
	R	0.171	0.087
	Δ_{rms}	0.281	0.004
Kendall τ	c/a ratio	0.058	0.388
	b/a ratio	0.077	0.255
	R	0.120	0.076
	Δ_{rms}	0.203	0.003
Spearman ρ	c/a ratio	0.093	0.357
	b/a ratio	0.115	0.252
	R	0.174	0.082
	Δ_{rms}	0.287	0.004

Table 9: Correlation statistics for WDM3 plane properties

With the statistics for Table 9, while I do see a similar trend as for Tables 7 and 8, I note the higher $p-$values as well. In WDM3, there is no longer a significant linear correlation between M and R, as could be seen for the previous two models. There is also a notable difference in the Pearson and Spearman statistics for R and Δ_{rms} when compared to the previous two models, in that the values show greater scatter (lower statistic values for WDM3 than for CDM and vSIDM). Similar to the previous two models, however, the equality of the Pearson and Spearman coefficients (Table 9) would indicate a scattered linear correlation if their p-values had been significant. Perhaps this is to be expected, given that the defining feature of WDM3 is the suppression of small-scale structures, including satellite planes. The model also results in satellite systems being more radially extended [50]. This is due to the fact that in WDM models, free-streaming prevents the formation of dense central cores, allowing dark matter to be distributed over a greater volume [50].

4.5 A Few Illustrative Plots

In this section, I present plots that correlate some of the quantities in a couple of different combinations to reinforce the results of the previous sections. In the first figure (Figure 18), I present plots for the b/a ratio against the c/a ratio for each model. In the second set of plots (Figure 19), I present the relative flattening (c/a ratio) against the kinematic coherence Δ_{sph}. Figure 18 is color-coded by the total number of luminous satellites per system, presented previously in Figure 8. Further, using values of b/a from [64], a region is shaded to indicate the literature value for the observed b/a for the eleven satellites of the Milky Way. Figure 19 is color-coded by Δ_{rms}, reflecting the absolute flattening of each plane in addition to the axis ratio on the $x-$ axis. The Milky Way itself is marked distinctly in red, using literature values for c/a and Δ_{sph} from [72].

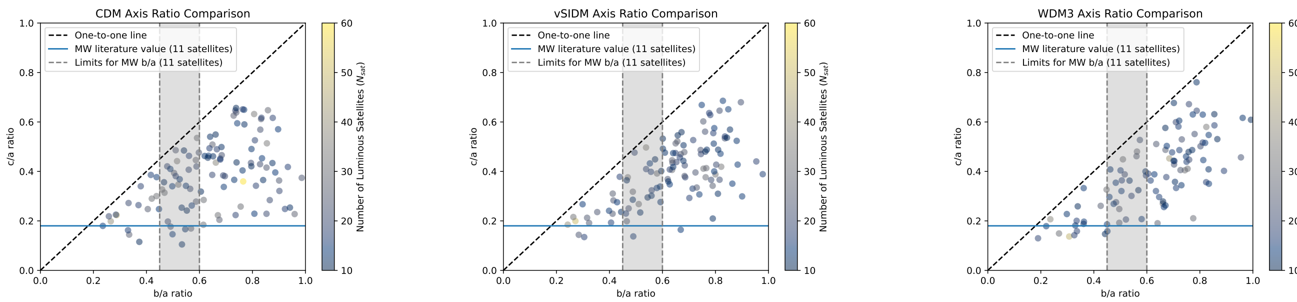

Figure 18: A plot of axis ratios, with b/a on the x-axis and c/a on the y-axis for CDM (left), vSIDM (center), and WDM3 (right). A black dotted line shows the one-to-one correspondence, and the blue line shows $c/a = 0.18$ for the Milky Way satellite system.

In Figure 18, very few of the simulated satellite systems fall on or under the blue line marking $c/a = 0.18$, the relative flattening of the Milky Way [38], [2]. This number is nine for CDM, four for vSIDM, and eight for WDM3, and they drop when also considering the shaded gray region (five, one, and one, respectively, for CDM, vSIDM, and WDM3). I report these numbers with the acknowledgment that while the Milky Way satellite plane consists of eleven satellites, the present work considers only ten (excluding the central subhalo). This skews the results slightly, as fewer points are more likely to produce flatter planes.

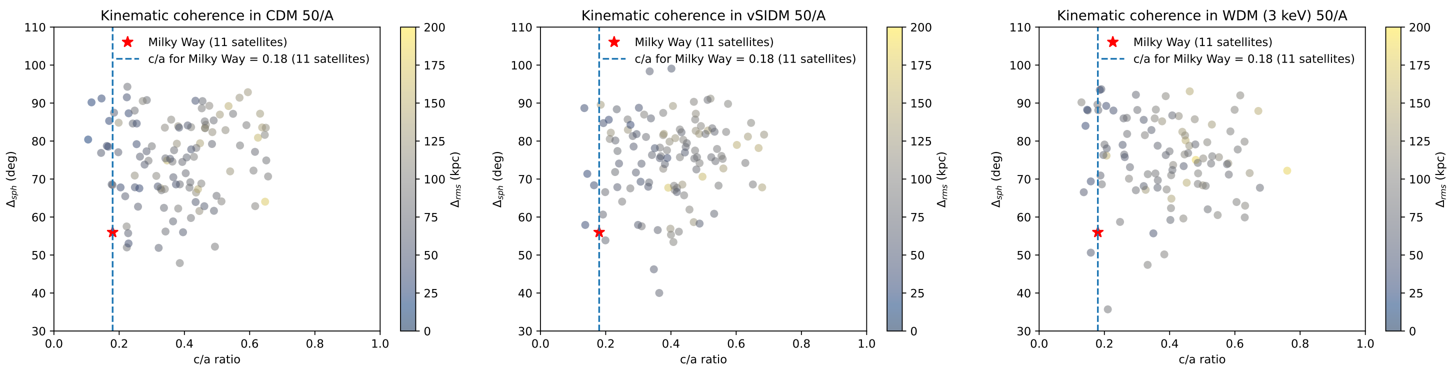

Figure 19: A plot illustrating kinematic coherence, with c/a on the x-axis and Δ_{sph} on the y-axis for CDM (left), vSIDM (center), and WDM3 (right). The blue line shows $c/a = 0.18$ for the Milky Way satellite system.

Figure 19 shows the scatter of the orbital pole dispersions with relative flattening. With a vertical line at $c/a = 0.18$ indicating the Milky Way value for 11 satellites (and the literature value for the Milky Way marked in red), we find that these systems do not show much (if any) kinematic coherence. In fact, in CDM, there is no system with a similar coherence as the Milky Way with the same level of flattening, and only a few points fall in the vicinity of the Milky Way in vSIDM and WDM3. This point further cements the results from Section 4.3, where it was established that (a) dark matter models do not change kinematic coherence significantly, (b) the systems do not move in a plane, and (c) the systems do not move in the best-fit plane, the metrics for which were presented in Sections 4.2 and 4.4. The plots presented here support the results of the previous sections that the choice of dark matter model has *no significant effect* on the frequency of occurrence of *kinematically coherent satellite planes.*

5 Conclusions and Avenues for Further Research

In answer to the research question posed in Section 1, whether the underlying dark matter model can affect the occurrence of satellite planes, I assessed three dark matter models: CDM, vSIDM, and WDM3. For the Milky Way analogs in the 51.7 kpc simulation box of the

AIDA-TNG simulations, I looked at four plane metrics: two measuring the relative flattening of the fit planes, the absolute thickness of the planes, and the radial extent of the plane. It was found that *the underlying dark matter model does not affect these plane properties significantly*, leading to the conclusion that *alternative dark matter models cannot produce satellite planes with more frequency than can CDM.*

I acknowledge the limitations of this research in a few areas. In addition to the three models assessed, AIDA-TNG also simulates a self-interacting dark matter model with a constant cross-section of particle interaction, and a warm dark matter model with a particle mass of 5 keV. This data was not available at the time of research at the same resolution as the data for the three models tested here. In the literature itself, there are several models of dark matter emerging. Reference [73] reviews more particle dark matter candidates.

A notable model is scalar-field or "fuzzy" dark matter, as introduced in [74]. According to [75], this model of dark matter treats entire galactic halos as atomic nuclei, to the effect of treating them using quantum mechanical equations usually used to explain the formation of molecules and bound and excited states. In this paradigm, satellite planes are explained as a consequence of an excited halo, as opposed to the ground state, where the default configuration would be a sphere (analogous to the s orbital in quantum mechanics). This scenario has not been tested in a cosmological simulation to the extent that other dark matter models have been tested. The reason for this is exactly this quantum mechanical nature that complicates numerical methods: quantum mechanics is notoriously difficult to code.

Nevertheless, the results reported in this work were expected. The dark matter models assessed here, in addition to the models simulated in [46], are motivated by solving small-scale challenges while preserving large-scale structure, to the end of reproducing the anisotropies observed in the cosmic microwave background (CMB). As such, their effect on the simulated halos (and therefore on satellite planes) was not expected to be significant. Even so, this result must be reported so that more models may be formulated and tested for their effects on other small-scale phenomena.

Future research can focus on larger sample sizes, extending beyond Milky Way analogs into higher and lower-mass regimes. According to [46], there is also higher resolution data to be released in the form of a smaller simulation box. More dark matter models may be assessed — not only for their cosmological implications, but also for small-scale dynamics such as the satellite planes phenomenon. If the explanation is to be found in any of these models, I am optimistic that it will be soon.

Appendix

Appendix A Algorithms

Determination of principal axes

Require: Parameters Vectors arranged in $[x_i, y_i, z_i]$ format to create an $N \times 3$ array. An individual vector shall be named **vec** and the full array shall be named **r**.

inertia_tensor $\leftarrow \vec{0}_3$ ▷ A 3×3 matrix of zeroes to start
for vec in **r do**
  $left \leftarrow$ DOT(**vec**, **vec**^{T}) $\times \mathbf{I}_3$ ▷ Where $\mathbf{I}_3$ is the 3×3 identity matrix
  $right \leftarrow$ MATRIX_PRODUCT(**vec**^{T}, **vec**)
  inertia_tensor $\leftarrow$ **inertia_tensor** $+ left + right$
  eig_vals, $eig\_vecs \leftarrow$ NUMPY.LINALG.EIG(**inertia_tensor**) ▷ This function is specific to Python, therefore any function that calculates the eigenvalues and the corresponding eigenvectors is sufficient.
  Declare empty dictionaries $index, norm, mag$ ▷ Any data structure that allows for key-value pairs and nested variations therein
  $index['a'] \leftarrow$ MINIMUM(eig_vals) ▷ The major axis is the axis corresponding to the *minimum* eigenvalue
  $index['c'] \leftarrow$ MAXIMUM(eig_vals) ▷ The minor axis is the axis corresponding to the *maximum* eigenvalue
  $index['b'] \leftarrow$Value within eig_vals that has not been assigned
  for $axis$ in a, b, c **do**
  $norm['axis'] \leftarrow eig\_vecs^T[index['axis']][0]$ ▷ The first value in the transposed eigenvectors array that is located at the index stored in $index['a']$
  $mag\_squared \leftarrow$ SUM(SQUARES(DOT(**vec**, $norm['axis']$))) ▷ The **vec** must loop over all values stored in **r**, regardless of if the value has been encountered in the outermost loop or not.
  $mag['axis'] \leftarrow$ SQRT($mag\_squared$/LENGTH(**r**))
  end for
  Construct a tensor of inertia dictionary **toi** that stores "key":$value$ pairs such that:
  "AxisA" : $norm['a']$ ▷ Unit vector in direction of major axis
  "AxisB" : $norm['b']$ ▷ Unit vector in direction of intermediate axis
  "AxisC" : $norm['c']$ ▷ Unit vector in direction of minor axis
  "MagA" : $mag['a']$ ▷ RMS heights of the points against the major axis
  "MagB" : $mag['b']$ ▷ RMS heights of the points against the intermediate axis
  "MagC" : $mag['c']$ ▷ RMS heights of the points against the minor axis
  "CARatio" : $mag['c']/mag['a']$ ▷ Axis ratio between minor and major axes
  "BARatio" : $mag['b']/mag['a']$ ▷ Axis ratio between intermediate and major axes
end for
return toi =0

Algorithm 1: The working of the tensor of inertia (TOI) function

Random Generation of Points

Require: Parameters Plane coefficients a, b, c, introduced standard deviation **thickness**, number of points to be generated **n_points** (default value set to 27)

z_axis $\leftarrow [0, 0, 1]$: Set the z-axis
$normal \leftarrow$ [**a, b, c**]: Create a Numpy array of the plane coefficients
$normalized \leftarrow$ [**a, b, c**]/NUMPY.LINALG.NORM($normal$): Normalized plane coefficients
$ang \leftarrow$ NUMPY.RANDOM.UNIFORM($0, 2\pi$, **n_points**) : Generate **n_points** number of random angular values. Setting up cylindrical coordinates.
$r \leftarrow$ NUMPY.RANDOM.UNIFORM($20, 250$, **n_points**) : Generate **n_points** number of random radial values. The upper and lower limits reflect the radial extent of the Milky Way's satellite plane in kpc.
Mapping cylindrical to Cartesian coordinates: $x \leftarrow r \times$ NUMPY.COS(ang), $y \leftarrow r \times$ NUMPY.SIN(ang)

$\boldsymbol{z} \leftarrow$ NUMPY.ZEROS(**n_points**) + NUMPY.RANDOM.NORMAL(**thickness**, **n_points**) : The $z-$ direction gets a Gaussian distribution, whose standard deviation is determined by the parameter **thickness**, which refers to the thickness of the generated artificial plane.

base_points $\leftarrow$ NUMPY.COLUMN_STACK($[\boldsymbol{x}, \boldsymbol{y}, \boldsymbol{z}]$) : We now have an array of **n_points** number of coordinates, arranged as a list of $[\boldsymbol{x}, \boldsymbol{y}, \boldsymbol{z}]$ values.

rot_axis $\leftarrow$ NUMPY.CROSS(***z_axis***, ***normalized***) : The cross product between the $z-$axis (normal to the $x - y$ plane) and the normalized plane coefficients returns the axis about which the ***base_points*** must be rotated.

rot_axis $\leftarrow$ ***rot_axis***/NUMPY.LINALG.NORM(***rot_axis***) : The unit vector in the direction of ***rot_axis***.

theta $\leftarrow$ NUMPY.ARCCOS(NUMPY.DOT(***normalized***, ***z_axis***)) : Finding the angle between the $z-$axis and the intended plane, so that ***base_points*** can be rotated.

$\mathbf{I} \leftarrow \mathbf{I}$, the 3×3 identity matrix.

if NUMPY.LINALG.NORM(***rot_axis***) $< 10^{-12}$ **then**

  return ***base_points*** : If the intended axis of rotation to get from the $z-$ axis to the intended plane normal is close to the $z-$axis below a certain tolerance, **do not rotate the points** and instead work with the points already randomly generated.

end if

Trigonometric functions for the rotation angle, for ease of rotation matrix calculation: ***costheta*** $\leftarrow$ NUMPY.COS(***theta***), ***sintheta*** $\leftarrow$ NUMPY.SIN(***theta***)

Setup of the $K-$matrix in Rodrigues Rotation Formula:

$$\boldsymbol{K} = \begin{bmatrix} 0 & -\boldsymbol{rot\_axis}[z] & \boldsymbol{rot\_axis}[y] \\ \boldsymbol{rot\_axis}[z] & 0 & -\boldsymbol{rot\_axis}[x] \\ -\boldsymbol{rot\_axis}[y] & \boldsymbol{rot\_axis}[x] & 0 \end{bmatrix}$$

Rodrigues Rotation Formula in matrix notation: $\boldsymbol{R} = \mathbf{I} + \boldsymbol{K} \times \boldsymbol{sintheta} + \boldsymbol{K}^2 \times (1 - \boldsymbol{costheta})$

$\boldsymbol{r\_rot} \leftarrow (\boldsymbol{R} \times \boldsymbol{base\_points}^T)^T$

return ***r_rot***

Algorithm 2: How to generate random points on an intended plane while introducing an artificial height

Testing the Inertia Tensor

1: **for** each iteration from 0 to 1999 **do**
2: $\quad$ $\mathbf{a, b, c}$ $\leftarrow$random number between $[1, 21)$
3: $\quad$ $\mathbf{scale}$ $\leftarrow$ random floating point number in range $[0, 100]$: This is a realistic range of Δ_{rms} generally seen in the simulation data
4: $\quad$ $\mathbf{mag} \leftarrow \sqrt{\mathbf{a}^2 + \mathbf{b}^2 + \mathbf{c}^2}$
5: $\quad$ $\boldsymbol{normal\_coeffs} \leftarrow [\mathbf{a, b, c}]$
6: $\quad$ $\boldsymbol{vecs} \leftarrow$ GENERATE_POINTS$(\mathbf{a, b, c, scale})$ $\quad$ ▷ Optional: Alter the default number of points from 27 to any desired number
7: $\quad$ $\boldsymbol{centroid} \leftarrow$ AVERAGE$(\boldsymbol{vecs})$
8: $\quad$ $\boldsymbol{centered} \leftarrow \boldsymbol{vecs} - \boldsymbol{centroid}$
9: $\quad$ $\boldsymbol{toi} \leftarrow$ INERTIA_TENSOR$(\boldsymbol{centered})$ $\quad$ ▷ **This is the function call to be tested**
10: $\quad$ Extract the following from the $\boldsymbol{toi}$ structure:
$\quad$ **AxisC**, **CARatio**, **BARatio**, **MagC**
11: $\quad$ $\boldsymbol{d} \leftarrow \mathbf{a} \times \boldsymbol{centroid_x} + \mathbf{b} \times \boldsymbol{centroid_y} + \mathbf{c} \times \boldsymbol{centroid_z}$ $\quad$ ▷ From the plane equation $Ax + By + Cz = D$; for the intended plane
12: $\quad$ $\boldsymbol{intended\_plane} \leftarrow [\mathbf{a, b, c}, \boldsymbol{d}]/\mathbf{mag}$
13: $\quad$ $\boldsymbol{d\_toi} \leftarrow \mathbf{AxisC_x} \times \boldsymbol{centroid_x} + \mathbf{AxisC_y} \times \boldsymbol{centroid_y} + \mathbf{AxisC_z} \times \boldsymbol{centroid_z}$ ▷ The value of D as calculated in **Step 10**, using plane coefficients returned by INTERTIA_TENSOR()
14: $\quad$ $\boldsymbol{toi\_plane} \leftarrow [\mathbf{AxisC_x}, \mathbf{AxisC_y}, \mathbf{AxisC_z}, \boldsymbol{d\_toi}]$
15: $\quad$ Create empty array $\boldsymbol{heights}$
16: $\quad$ **for** Each $\boldsymbol{point}$ in $\boldsymbol{vecs}$ **do**
17: $\quad\quad$ $\boldsymbol{num} \leftarrow |DOT(\boldsymbol{normal_coeffs}, \boldsymbol{point}) - \boldsymbol{d}|$
18: $\quad\quad$ $\boldsymbol{den} \leftarrow \mathbf{mag}$
19: $\quad\quad$ $\boldsymbol{height} \leftarrow \boldsymbol{num}/\boldsymbol{den}$
20: $\quad\quad$ $\boldsymbol{heights} \leftarrow \boldsymbol{height}$
21: $\quad$ **end for**
22: $\quad$ $\boldsymbol{rms\_heights} \leftarrow$ SQRT(MEAN(SQUARE$(\boldsymbol{heights})$)) $\quad$ ▷ Δ_{rms} for the intended plane are calculated manually to compare against **MagC** returned by INTERTIA_TENSOR().
23: $\quad$ $\boldsymbol{angle} =$ ARCCOS(DOT$(\boldsymbol{normal_coeffs}/\mathbf{mag}, \mathbf{AxisC})$) $\quad$ ▷ A way to compare the intended and fit plane coefficients: The lower the value, the closer the match.
24: $\quad$ Record in output file: iteration number, $\mathbf{a, b, c}$, $\mathbf{a/mag, b/mag, c/mag}$, **AxisC**, **CARatio**, **BARatio**, **MagC**, $\boldsymbol{rms\_heights}$, $\boldsymbol{angle}$, **scale**, $\boldsymbol{centroid}$
25: **end for**

Algorithm 3: Testing Algorithm 1 on randomly generated points

General Data Processing

1: Load the simulation data for the relevant model
2: Make the first cut: Identify all the Milky Way analogs and the subhalos bound therein (Figure 2, step 2)
3: Make the second cut: Identify the subhalos within the first cut where the subhalos have a non-zero stellar mass, **and** are dark matter dominated (Figure 2, step 3). This yields a dictionary in the same format as the full dataset loaded in Step 1, but only for Milky Way analogs and luminous subhalos.
4: Get the following dictionaries:
$\quad$ GroupNr: subhalo coordinates
$\quad$ GroupNr: stellar mass of each subhalo
$\quad$ GroupNr: coordinates of central subhalo
$\quad$ GroupNr: velocities of each subhalo
5: Use the group numbers (**SubhaloGrNr**) as a primary key to access various satellite systems
6: **for** key **in** GroupNr **do**
7: $\quad$ **if** count(coordinates) > 10 **then**
8: $\quad\quad$ Extract the list of coordinates from the dictionary
9: $\quad\quad$ Extract the position of the central subhalo
10: $\quad\quad$ Remove the central subhalo position from the full set of coordinates, and

remove any coordinates whose magnitude > 10 kpc. The length of the resulting array is $\mathbf{N_{sat}}$, recorded in the output file.

11: Using a library-defined function and Equation 1, extract the top ten luminous subhalos for this system, centered around the central subhalo. Also store the relative velocities of these subhalos.

12: Using Equation 2 encoded into a library function, calculate the centroid of the distribution (Step 11). Record **d** to store as the centroid offset.

13: Using Equation 2 encoded into a second library function, center the distribution (step 11) around the centroid.

14: Apply INTERTIA_TENSOR(), defined in the library, to the distributions yielded in Step 11 and Step 13. Record the following:
Unit vector of the thinnest plane (as a variable), and
$\mathbf{\Delta_{rms}}$, $\mathbf{c/a}$, and $\mathbf{b/a}$ in the output file for both distributions.

15: Using the plane equation $Ax+By+Cz = D$, and the origin (as we are working with centroid-centered and host-centered coordinates), evaluate D. The function to do so is included in the overarching library.

16: Calculate and record **R**, the RMS radial extent. (Function included in library.)

17: Calculate and record $\boldsymbol{\theta}$ (Table 1), stored as both radians and degrees. (Function included in library.)

18: Use a separate library function to calculate $\mathbf{\Delta_{rms}}$ for both distributions (Step 11, Step 13). Record as output.

19: From the position and velocity data (Step 11), calculate the specific angular momentum, orbital pole (Equation 4), and θ_{rms} (Equation 16 using the $\mathbf{+n}$ direction.

20: Repeat Step 19 for the $\mathbf{-n}$ direction.

21: **if** θ_{rms}^{-n} ¡ θ_{rms}^{+n} **then**
Calculate orbital pole dispersion using the $\mathbf{-n}$ direction of the plane normal. Also plot the Mollweide all-sky maps for the clustering of angular momenta, positions, and velocities of the satellites.

22: **else**
Calculate orbital pole dispersion using the $\mathbf{+n}$ direction of the plane normal. Also plot the Mollweide all-sky maps for the clustering of angular momenta, positions, and velocities of the satellites.

23: **end if**

24: Using a defined library function that encodes Equation 15, calculate and record the plane offset.

25: Use a specially defined library function to plot the host-centered distribution (Step 11), the plane fits for both distributions, and the centroid. This plot is saved as an interactive HTML file.

26: **end if**

27: **end for**

Algorithm 4: Applying plane fitting procedures, using specialized library functions and previously defined algorithms, to the dark matter models

Comparing Simulation Data to a Random Distribution

1: Store the CDM, vSIDM, and WDM3 radial and velocity samples as $N \times 10$ arrays.

2: **for** 1000 runs **do**

3: Choose one random radial distribution for each dark matter model.

4: Choose the corresponding velocity distribution.

5: Randomize $\boldsymbol{\theta}$ and $\boldsymbol{\phi}$ to create an isotropic distribution with random velocity vectors, following Equation 17.

6: Follow Algorithm 4, steps 14—24, to record c/a, b/a, Δ_{rms}, R, θ_{rms}, and Δ_{sph}.

7: Store the results for all three dark matter models in separate output files.

8: **end for**

Algorithm 5: Creating and evaluating a random distribution. This algorithm creates an isotropic distribution from pre-existing simulation data.

Appendix B Data Access

B.1 Simulation Data and Relevance to Project

Field	Description according to Illustris-TNG Documentation [3]	Relevance
'halos' "Group_M_Crit200"	Total Mass of this group enclosed in a sphere whose mean density is 200 times the critical density of the Universe, at the time the halo is considered.	Filtering halos whose masses are analogous to the mass of the Milky Way; Plotting plane properties to determine correlations
'subhalos' 'SubhaloGrNr"	Index into the Group table of the FOF host/parent of this Subhalo.	Primary key to index halos and link the 'halos' and 'subhalos' datasets. Determine which subhalos belong to which halos.
'subhalos' "Subhalo-MassType" [:, 4]	Total mass of all member particle/cells which are bound to this Subhalo, separated by type, with 4 being the type for stellar mass.	Identifying subhalos with stellar mass > 0 and determination of luminosity rankings within groups
'subhalos' "Subhalo-MassType" [:, 1]	As above, but where 1 now refers to dark matter particles.	Determination of dark matter dominance of subhalos, so as not to accidentally include disk fragments.
'subhalos' "SubhaloMass"	Total mass of all member particle/cells which are bound to this Subhalo, of all types.	Determination of dark matter dominance, in conjunction with the above.
'subhalo' "SubhaloPos"	Spatial position within the periodic box (of the particle with the minimum gravitational potential energy). Comoving coordinate.	Plane fitting, plotting, and some data selection.
'halos' "GroupFirstSub"	Index into the 'Subhalo' table of the first (i.e., central/primary) Subfind subhalo within this FoF group.	Determination of central subhalo to center coordinates in the host-centered frame.
'header' "BoxSize"	Spatial extent of the periodic box (in comoving units).	Application of the periodic boundary corrections (Equation 1).
'subhalos' "SubhaloVel"	Peculiar velocity of the group, computed as the sum of the mass-weighted velocities of all particles/cells in this group, of all types. No unit conversion is needed.	Determination of the kinematics of the subhalos and resulting satellite planes, e.g., specific angular momenta, orbital poles, alignment to spatial distribution.

Table 10: Summary of simulation data fields used in the present analysis. The second column is credited to the data specifications of Illustris-TNG [3].

B.2 Full list of variable names and their meanings

Variable	Meaning	Algorithm 4 Step
GrNr	Index of the host system currently being evaluated in the full dataset	5
N_{sat}	Number of subhalos identified for this system, excluding the central subhalo and those within 10 kpc of the central subhalo	10
d	Centroid offset, Equation 2 (kpc)	12
$d_\perp$	Plane offset, Equation 15 (kpc)	24
$(c/a)_c$	Minor-to-major axis ratio for the plane fit in the centroid-centered frame	14
$(b/a)_c$	Intermediate-to-major axis ratio for the plane fit in the centroid-centered frame	14
$\Delta_{rms}^{c,TOI}$	RMS height returned by the TOI function for the centroid-centered plane fit (kpc)	14
$(c/a)_h$	Minor-to-major axis ratio for the plane fit in the host-centered frame	14
$(b/a)_h$	Intermediate-to-major axis ratio for the plane fit in the host-centered frame	14
$\Delta_{rms}^{h,TOI}$	RMS height returned by the TOI function for the host-centered plane fit (kpc)	14
R_c	RMS radial extent for the centroid-centered frame (kpc)	16
R	RMS radial extent for the host-centered frame, used for further data analysis (kpc)	16
θ_{rad}	Angle between the plane fits in both frames, radians	17
θ	Angle between the plane fits in both frames, deg, used for further data analysis	17
$\Delta_{rms}^{c,calc}$	RMS height calculated by a library-defined function in the centroid-centered frame, kpc	18
$\Delta_{rms}^{h,calc}$	RMS height calculated by a library-defined function in the host-centered frame, kpc	18
$\vec{h}$	Specific angular momentum, Equation 4, in kpc km/s	19, 20
$\hat{h}$	Orbital pole, Equation 4, in kpc km/s	19, 20
θ_{rms}	The RMS angle between $\hat{h}$ and the plane normal $\mathbf{n}$. Two values are calculated: once against $+\mathbf{n}$, and once against $-\mathbf{n}$. The smaller value is used for further analysis. Reported in degrees.	19, 20
$\Delta_{sph}(k)$	Orbital pole dispersion, indicating the clustering of orbital poles. Reported in degrees. $k = 10$ implicitly assumed in main text.	21, 22

Table 11: Variables recorded in the output files for further data analysis

Appendix C Library Function Documentation and Some Example Outputs

- $h = 0.6774$ is the reduced Hubble constant (Equation 14).
- `sim_to_solar_mass (mass)`: The AIDA-TNG and Illustris-TNG simulation data are stored in units of $10^{10}/h$ solar masses. This function multiplies the simulation data by that factor, so that the masses I work with are the standard solar mass units (Equation 14).
- `coordinates_present_day(dist, a=1)`: Any quantity with dimension [L] in the AIDA-TNG simulations is reported in comoving kiloparsecs, ckpc/h. According to the Illustris-

TNG documentation, the conversion to present-day coordinates is done as (present) = (comoving) $*$ scale factor/h. The reduced Hubble constant h is predefined in this library. Since the dataset deals with current conditions and does not assess evolution, the scale factor is set to 1. This function performs the conversion from comoving coordinates — taken as the function parameter — to present-day coordinates, reporting the output in kpc. The function is suitable for individual numbers as well as array-like structures.

- `filter_halo_mass(fulldict)`: This function takes an AIDA-TNG dictionary with the FULL details of the simulation run: halo, headers, and subhalos. It returns a dictionary filtered by Milky Way analogs: halo masses between 0.8 and 3×10^{12} solar masses. The returned dictionary has the same layout as the dictionary originally loaded from the AIDA-TNG data. Subhalos belonging to the Milky Way analogs are also identified.
- `stellarmassfilter(filtereddict)`: Not all subhalos around the halos will have luminous (stellar) mass. This function takes a dictionary of Milky Way analogs (can also take other dictionaries), and filters out the subhalos that have a non-zero stellar mass. This way, I am working with only luminous subhalos. Second check added to ensure subhalos are also dark matter dominated, so that certain subhalos are not suspected to be disk fragments of the host.
- `group_by_grNr(stellarfilter)`: With a dictionary that has Milky Way analogs and information on only the luminous subhalos, this function sorts which subhalos belong to which halos. For the set of subhalos belonging to a halo, this function returns a dictionary with the coordinates (c kpc / h) of the subhalos of each group, and the masses (solar units) of those subhalos. This is done to make a one-to-one mapping between the coordinates and masses of the same subhalo easier for center-of-mass calculations. With each new update, the function returns more dictionaries that group the grNr with other quantities of interest, like host halo position.
- `haloposdict(stellardict, fulldict)`: This function accesses the entry GroupFirstSub of the filtered halos. The GroupFirstSub entry is an index pointing to the central subhalo for a given group in the unfiltered dictionary. This index is then used to access the position and SubhaloGrNr of the central subhalo from the unfiltered dict, creating a key: value pair in the form of SubhaloGrNr: SubhaloPos, returned to the main program.
- `center_coords_by_halo(coords, halopos, boxsize)`: In a classic shifting of the origin problem, this function accepts a list of coordinates $(N, 3)$, and the position of the halo, to center the raw simulation data coordinates around the halo, treating the halo as the origin. The function returns another $(N, 3)$ array of (x, y, z) values of coordinates so centered. Updated algorithm credit to Abhilash Sengupta: Function now accounts for the periodic boundary based on the box size of the simulation.
- `relative_vel(all_vels, central_vel)`: Takes as input the velocities of all subhalos, and the velocity of the central subhalo, and returns the relative velocities of the subhalos from the reference frame of the central subhalo. As these orbital velocities are well under the relativistic threshold, the Galilean transformation is used. All units used are km/s.
- `top10luminous(key, stellarfilter, fulldict)`: This function returns the top 10 luminous subhalos within each group, given the key (SubhaloGrNr), the catalog of the stellar subhalos, and the full catalog loaded from the AIDA-TNG data. The returned points are centered around the central subhalo, and at a distance greater than 10 kpc from the central subhalo. The velocities corresponding to these positions, relative to the central subhalo, are also returned.
- `get_avg(coords)`: This function takes in a list of coordinates $(N, 3)$ and returns their arithmetic mean.
- `center_coords_byavg(coords)`: In a classic shifting of the origin problem, this function accepts a list of coordinates $(N, 3)$, and the average of the coordinates, to center the halo-centered coordinates around their mean, treating the mean as the origin. The function returns another $(N, 3)$ array of (x, y, z) values of coordinates so centered.

- `inertia_tensor(r)`: (Credit: Marcel Pawlowski, Mariana Júlio, K. Jamie Kanehisa) This function takes in a list of vectors stored in (x, y, z) format (shape $N, 3$) and calculates unit vectors for the axis of thickest, thinnest, and intermediate flattening. It returns a unit vector that is *normal* to the thinnest plane, essentially giving A, B, and C values for a plane fit.

- `equation_of_plane(normal1, normal2, x_avg, y_avg, z_avg, halocoords)`: The inertia_tensor() function is called to operate on the centered coordinates. The returned values are stored in the parameter normal, passed to this function. Along with the centroid-centered coordinates, this information is used to solve for D in the plane equation $Ax + By + Cz = D$. The values A, B, C, D are returned to the user. Two planes are returned to the user: one forced through the mean of the points, and one forced through the halo.

- `plane_offset(plane_av, host_in_av_frame)`: Calculate the distance of the host from the plane forced through the centroid. To do this, I operate in the centroid-centered frame of reference, where the plane coefficients run through the origin, and the position of the host is simply -(centroid). Both parameters are expected to be passed as a tuple, list, or similar. The plane equation used is $Ax + By + Cz = D$, not assumed to be normalized. Normalization is handled in this function.

- `specific_ang_momenta_alignment(positions, velocities, plane_norm)`: Computes the specific angular momentum $\mathbf{r} \times \vec{v}$ to return to the user. It also computes the alignment of the orbital pole (unit vector of specific angular momentum) with the plane normal, yielding angular values in degrees (not returned to user). Finally, the RMS alignment of the orbital pole is calculated, the value returned to be stored.

- `orb_pole_disp(L_hat, n_sat=10)`: The orbital pole dispersion is an RMS value. To calculate it, I first take the mean orbital pole. Then, I measure the angle between the individual orbital poles and the mean orbital pole. The RMS value of these angles is returned to the user. I work with degrees.

- `all_sky_L_map(centeredpos, ang_mom, plane_norm, save_path)`: Creates and saves an all-sky map (Mollweide projection) of the angular momenta of the subhalos (central subhalo at origin), color-coded by alignment of the orbital pole to the plane normal, passed here as a unit vector. The points are rotated such that the plane normal points to $(1, 0, 0)$: in Mollweide, directly out of the page (or screen, as it were).

- `all_sky_v_map(centeredpos, ang_mom, plane_norm, velocities, save_path)`: Saves quiver plots of the Mollweide projections. The points are now the centered coordinates, rotated so that the plane normal points directly out of the page (or screen), and color coded by the value of $\hat{h} \cdot \mathbf{n}$. Arrows point to the velocity vector in the same projection.

- `graph_and_save(coords, plane1, plane2, x_av, y_av, z_av, halo_coords, save_static, save_html)`: Plots a 3D scatter of points (centering determined by the user) and the fitted planes, and can save both a static PNG and an interactive HTML plot.

- `angle_between_planes(plane1, plane2)`: This function calculates the angle between two planes. This is useful when the plane fits from the centroid-centered coordinates host-centered coordinates are at an incline towards each other, and will be used for data analysis further. The order of the planes — halo first or average first — does not matter here. Plane equation used here is $ax + by + cz = -d$, but the formula itself is independent of d.

- `get_rms_heights(coords_a, plane_a, coords_h, plane_h)`: Calculate the RMS heights of the coordinates centered around the centroid to the plane forced through the centroid, and similarly for the coordinates and plane that center around the host halo. Returns two RMS height values.

- `getrmsradial(dist)`: Calculates the RMS radial extent of the satellite plane, based on the magnitudes of the centered coordinates.

A sample output

```
GrNr 42
Number of satellites = 59
Distance between GroupFirstSub and average point = 229.2743757640514 kpc
Final satellite Count = 59
Average centered c/a = 0.41510604192048584
Average centered b/a = 0.8058564573706429
Returned RMS height from TOI fn (average centered) = 96.93800417140288 kpc
Host centered c/a = 0.3595144623148971
Host centered b/a = 0.7651157494535344
Returned RMS height from TOI fn (host centered) = 107.01030599206018 kpc
RMS radial extent (average centered) = 315.1922912597656 kpc
RMS radial extent (host centered) = 389.7600402832031 kpc
Incline between planes (rad) = 0.22912596440880417
Incline between planes (deg) = 13.127950737489186
RMS height by average = 96.93800417140288 kpc
RMS height by halo = 107.01030599206018 kpc
Orbital Pole Dispersion (deg) = 85.63493555494743
RMS scatter away from normal (deg) = 96.13132748286527
Plane offset (kpc) = 76.70308499046799
```

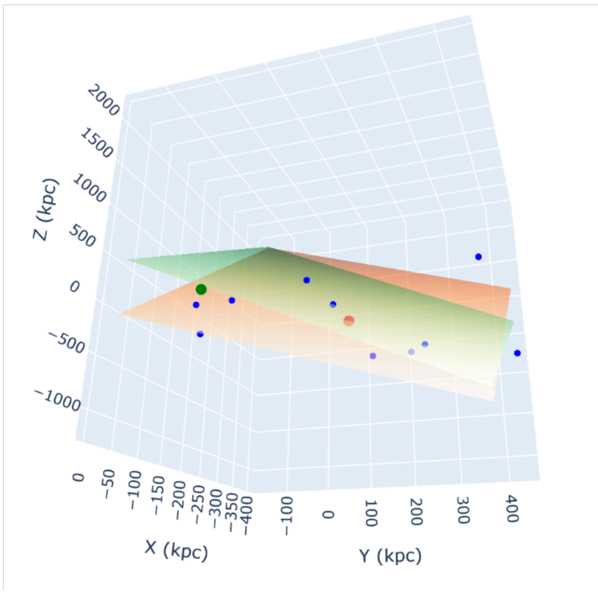

Figure 20: The plot corresponding to the text output. The green plane, seen nearly edge-on, is the host-centered plane. The orange plane is the centroid-centered plane. The host — central subhalo — is the large green dot. The centroid is positioned relative to the host. The blue points show the top 10 luminous satellites, all centered around the host.

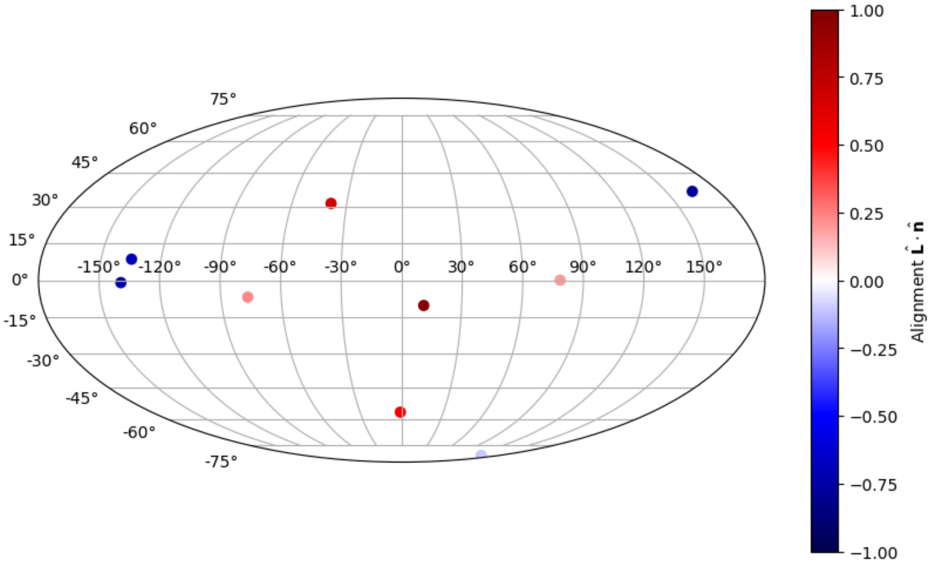

Figure 21: All-sky map for the direction of the angular momentum vector, color coded by its alignment to the plane normal. This plot is in the Mollweide projection.

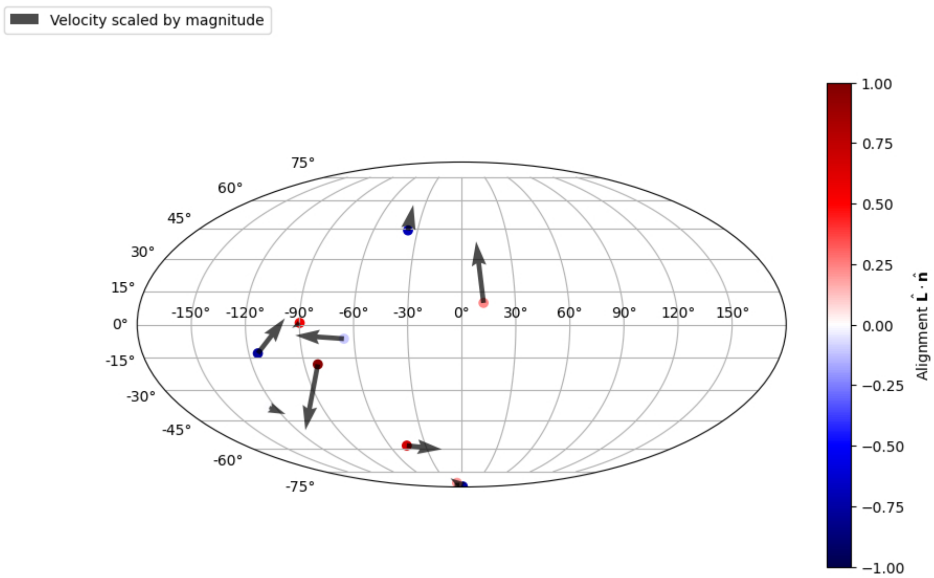

Figure 22: All-sky map for the positions (dots) and velocity vectors (arrows anchored on the dots), color coded by the alignment of the angular momentum to the plane normal for each individual dot. This plot is in the Mollweide projection.

References

[1] M. S. Roberts and A. H. Rots. Comparison of Rotation Curves of Different Galaxy Types. , 26:483–485, August 1973.

[2] Xinghai Zhao, Guobao Tang, Paola Gonzalez, Grant J. Mathews, and Lara Arielle Phillips. Analysis of the plane of satellites around milky way-like galaxies in λcdm cosmology, 2025.

[3] Dylan Nelson, Volker Springel, Annalisa Pillepich, Vicente Rodriguez-Gomez, Paul Torrey, Shy Genel, Mark Vogelsberger, Ruediger Pakmor, Federico Marinacci, Rainer Weinberger, Luke Kelley, Mark Lovell, Benedikt Diemer, and Lars Hernquist. The illustristng simulations: Public data release, 2021.

[4] Harlow Shapley and Heber D. Curtis. The Scale of the Universe. *Bulletin of the National Research Council*, 2(11):171–217, May 1921.

[5] Heinz Andernach and Fritz Zwicky. English and Spanish Translation of Zwicky's (1933) The Redshift of Extragalactic Nebulae. *arXiv e-prints*, page arXiv:1711.01693, November 2017.

[6] J. H. Oort. Some Problems Concerning the Structure and Dynamics of the Galactic System and the Elliptical Nebulae NGC 3115 and 4494. , 91:273, April 1940.

[7] Joachim Wambsganss. Gravitational Lensing in Astronomy. *Living Reviews in Relativity*, 1(1):12, December 1998.

[8] Shude Mao and Bohdan Paczynski. Mass Determination with Gravitational Microlensing. , 473:57, December 1996.

[9] Yoshiaki Sofue and Vera Rubin. Rotation curves of spiral galaxies. *Annual Review of Astronomy and Astrophysics*, 39(1):137–174, 2001.

[10] Julio F. Navarro, Carlos S. Frenk, and Simon D. M. White. The Structure of Cold Dark Matter Halos. , 462:563, May 1996.

[11] G. Gentile, P. Salucci, U. Klein, D. Vergani, and P. Kalberla. The cored distribution of dark matter in spiral galaxies. *Monthly Notices of the Royal Astronomical Society*, 351(3):903–922, 07 2004.

[12] David Merritt, Alister W. Graham, Ben Moore, Jürg Diemand, and Balša Terzić. Empirical models for dark matter halos. i. nonparametric construction of density profiles and comparison with parametric models. *The Astronomical Journal*, 132(6):2685, nov 2006.

[13] Tilman Sauer. Albert einstein's 1916 review article on general relativity, 2004.

[14] Tereasa G. Brainerd, Roger D. Blandford, and Ian Smail. Weak gravitational lensing by galaxies. *The Astrophysical Journal*, 466:623, August 1996.

[15] Sabine Schindler. Ω_m - Different Ways to Determine the Matter Density of the Universe. , 100:299–309, January 2002.

[16] Iminhaji Ablimit, Gang Zhao, Chris Flynn, and Sarah A. Bird. The Rotation Curve, Mass Distribution, and Dark Matter Content of the Milky Way from Classical Cepheids. , 895(1):L12, May 2020.

[17] Yoshiaki Sofue. Rotation Curve of the Milky Way and the Dark Matter Density. *Galaxies*, 8(2):37, April 2020.

[18] R. Sadat. Influence of the Non-Luminous Component on Dynamical and Structural Properties of Galaxy Clusters. Does X-Ray Gas Mimic the Missing Mass? , 234(2):303–323, December 1995.

[19] Douglas Clowe, Anthony Gonzalez, and Maxim Markevitch. Weak-Lensing Mass Reconstruction of the Interacting Cluster 1E 0657-558: Direct Evidence for the Existence of Dark Matter. , 604(2):596–603, April 2004.

[20] Annika H. G. Peter. Dark Matter: A Brief Review. *arXiv e-prints*, page arXiv:1201.3942, January 2012.

[21] G. R. Blumenthal, S. M. Faber, J. R. Primack, and M. Rees. Formation of Galaxies and Large-Scale Structure with Cold Dark Matter. In Edward W. Kolb and Michael S. Turner, editors, *The Early Universe: Reprints*, page 617. Unknown, 1988.

[22] Katherine Freese, Brian Fields, and David Graff. Death of Stellar Baryonic Dark Matter Candidates. *arXiv e-prints*, pages astro–ph/0007444, July 2000.

[23] M. Milgrom. A modification of the Newtonian dynamics as a possible alternative to the hidden mass hypothesis. , 270:365–370, July 1983.

[24] S. T. Nagesh, J. Freundlich, B. Famaey, and M. Bilek. Galaxy clusters in MOND: the case of ultra diffuse galaxies in the Coma cluster. In M. N'Diaye, A. Siebert, N. Lagarde, O. Venot, K. Baillié, M. Béthermin, E. Lagadec, J. Malzac, and J. Richard, editors, *SF2A-2023: Proceedings of the Annual meeting of the French Society of Astronomy and Astrophysics*, pages 63–66, December 2023.

[25] S. Planelles, D. R. G. Schleicher, and A. M. Bykov. Large-scale structure formation: From the first non-linear objects to massive galaxy clusters. *Space Science Reviews*, 188(1-4):93–139, April 2014.

[26] Rita Tojeiro and Katarina Kraljic. Large Scale Structure and the Cosmic Web. *arXiv e-prints*, page arXiv:2503.21759, March 2025.

[27] R. H. Dicke, P. J. E. Peebles, P. G. Roll, and D. T. Wilkinson. Cosmic Black-Body Radiation. , 142:414–419, July 1965.

[28] Tarun Souradeep, Rajib Saha, and Pankaj Jain. Angular power spectrum of CMB anisotropy from WMAP. , 50(11-12):854–860, December 2006.

[29] Bruce A. Bassett and Renée Hlozek. Baryon acoustic oscillations, 2009.

[30] George Ellis. The Standard Cosmological Model: Achievements and Issues. *Foundations of Physics*, 48(10):1226–1245, October 2018.

[31] James S. Bullock and Michael Boylan-Kolchin. Small-Scale Challenges to the ΛCDM Paradigm. , 55(1):343–387, August 2017.

[32] Laura V. Sales, Andrew Wetzel, and Azadeh Fattahi. Baryonic solutions and challenges for cosmological models of dwarf galaxies. *Nature Astronomy*, 6:897–910, June 2022.

[33] Ben Moore, Sebastiano Ghigna, Fabio Governato, George Lake, Thomas Quinn, Joachim Stadel, and Paolo Tozzi. Dark matter substructure within galactic halos. *The Astrophysical Journal*, 524(1):L19–L22, October 1999.

[34] Ilin Lazar, Sugata Kaviraj, Garreth Martin, Aaron Watkins, Darshan Kakkad, Brian Bichang'a, Katarina Kraljic, Sukyoung K. Yi, Yohan Dubois, Julien E. G. Devriendt, Sebastien Peirani, and Christophe Pichon. The dwarf stellar mass function in different environments and the lack of a generic missing dwarfs problem in Λcdm, 2025.

[35] W. J. G. de Blok. The core-cusp problem. *Advances in Astronomy*, 2010(1), November 2009.

[36] Michael Boylan-Kolchin, James S. Bullock, and Manoj Kaplinghat. Too big to fail? the puzzling darkness of massive milky way subhaloes. *Monthly Notices of the Royal Astronomical Society: Letters*, 415(1):L40–L44, 2011.

[37] Michael Boylan-Kolchin, James S. Bullock, and Manoj Kaplinghat. The Milky Way's bright satellites as an apparent failure of ΛCDM. , 422(2):1203–1218, May 2012.

[38] Marcel S. Pawlowski. The planes of satellite galaxies problem, suggested solutions, and open questions. *Modern Physics Letters A*, 33(6):1830004, February 2018.

[39] David Martinez-Delgado, Michael Stein, Marcel S. Pawlowski, Joanna D. Sakowska, Dmitry Makarov, Lidia Makarova, Giuseppe Donatiello, and Dustin Lang. Tracing satellite planes in the sculptor group: Ii. discovery of five faint dwarf galaxies in the desi legacy survey, 2025.

[40] Till Sawala, Marius Cautun, Carlos Frenk, John Helly, Jens Jasche, Adrian Jenkins, Peter H. Johansson, Guilhem Lavaux, Stuart McAlpine, and Matthieu Schaller. The Milky Way's plane of satellites is consistent with ΛCDM. *Nature Astronomy*, 7:481–491, April 2023.

[41] Marcel S. Pawlowski. Phase-Space Correlations among Systems of Satellite Galaxies. *Galaxies*, 9(3):66, September 2021.

[42] C. Welker, Y. Dubois, C. Pichon, J. Devriendt, and N. E. Chisari. Caught in the rhythm. I. How satellites settle into a plane around their central galaxy. , 613:A4, May 2018.

[43] Janvi P. Madhani, Charlotte Welker, Sneha Nair, Daniel Gallego, Lianys Feliciano, Christophe Pichon, Charlotte Olsen, Yohan Dubois, Sugata Kaviraj, and Katarina Kraljic. Zippers and twisters: Planes of satellite galaxies emerge from whirling and shocking gas streams in the cosmic web, 2026.

[44] Mariana P. Júlio, Marcel S. Pawlowski, Sangmo Tony Sohn, Salvatore Taibi, Roeland P. van der Marel, and Stacy S. McGaugh. Satellite group infall into the Milky Way: Exploring the Crater-Leo case with new HST proper motions. , 687:A212, July 2024.

[45] Indranil Banik, David O'Ryan, and Hongsheng Zhao. Origin of the Local Group satellite planes. , 477(4):4768–4791, July 2018.

[46] Giulia Despali, Lauro Moscardini, Dylan Nelson, Annalisa Pillepich, Volker Springel, and Mark Vogelsberger. Introducing the AIDA-TNG project: Galaxy formation in alternative dark matter models. , 697:A213, May 2025.

[47] Joel R. Primack. Galaxy Formation in ΛCDM Cosmology. *Annual Review of Nuclear and Particle Science*, 74(1):173–206, June 2024.

[48] Gianfranco Bertone, Djuna Croon, Mustafa Amin, Kimberly K. Boddy, Bradley Kavanagh, Katherine J. Mack, Priyamvada Natarajan, Toby Opferkuch, Katelin Schutz, Volodymyr Takhistov, Christoph Weniger, and Tien-Tien Yu. Gravitational wave probes of dark matter: challenges and opportunities. *SciPost Physics Core*, 3(2):007, October 2020.

[49] Gianfranco Bertone, Dan Hooper, and Joseph Silk. Particle dark matter: evidence, candidates and constraints. , 405(5-6):279–390, January 2005.

[50] Paul Bode, Jeremiah P. Ostriker, and Neil Turok. Halo Formation in Warm Dark Matter Models. , 556(1):93–107, July 2001.

[51] Sean Tulin and Hai-Bo Yu. Dark matter self-interactions and small scale structure. , 730:1–57, February 2018.

[52] Annalisa Pillepich, Volker Springel, Dylan Nelson, Shy Genel, Jill Naiman, Rüdiger Pakmor, Lars Hernquist, Paul Torrey, Mark Vogelsberger, Rainer Weinberger, and Federico Marinacci. Simulating galaxy formation with the IllustrisTNG model. , 473(3):4077–4106, January 2018.

[53] Rainer Weinberger, Volker Springel, and Rüdiger Pakmor. The AREPO Public Code Release. , 248(2):32, June 2020.

[54] Ulrich K. Deiters. Efficient coding of the minimum image convention, March 2013.

[55] M. Vogelsberger, S. Genel, V. Springel, P. Torrey, D. Sijacki, D. Xu, G. Snyder, S. Bird, D. Nelson, and L. Hernquist. Properties of galaxies reproduced by a hydrodynamic simulation. , 509(7499):177–182, May 2014.

[56] E. L. Turner and J. R. Gott, III. Groups of galaxies. I. A catalog. , 32:409–427, November 1976.

[57] Volker Springel, Simon D. M. White, Giuseppe Tormen, and Guinevere Kauffmann. Populating a cluster of galaxies – i. results at z = 0. *Monthly Notices of the Royal Astronomical Society*, 328(3):726–750, 12 2001.

[58] Gustavo E. Medina et al. The mass of the Milky Way from outer halo stars measured by DESI DR1. *arXiv e-prints*, page arXiv:2508.19351, August 2025.

[59] Thomas M Callingham, Marius Cautun, Alis J Deason, Carlos S Frenk, Wenting Wang, Facundo A Gómez, Robert J J Grand, Federico Marinacci, and Ruediger Pakmor. The mass of the milky way from satellite dynamics. *Monthly Notices of the Royal Astronomical Society*, 484(4):5453–5467, February 2019.

[60] Laura L. Watkins, N. Wyn Evans, and Jin H. An. The masses of the Milky Way and Andromeda galaxies. , 406(1):264–278, July 2010.

[61] K. J. Fushimi, M. E. Mosquera, and M. Dominguez. A determination of the Large Magellanic Cloud dark matter subhalo mass using the Milky Way halo stars in its gravitational wake. , 688:A147, August 2024.

[62] Laura L. Watkins, Roeland P. van der Marel, and Paul Bennet. The Mass of the Large Magellanic Cloud from the Three-dimensional Kinematics of Its Globular Clusters. , 963(2):84, March 2024.

[63] N. F. Martin, R. A. Ibata, M. Bellazzini, M. J. Irwin, G. F. Lewis, and W. Dehnen. A dwarf galaxy remnant in Canis Major: the fossil of an in-plane accretion on to the Milky Way. , 348(1):12–23, February 2004.

[64] Manuel Metz, Pavel Kroupa, and Helmut Jerjen. The spatial distribution of the Milky Way and Andromeda satellite galaxies. , 374(3):1125–1145, January 2007.

[65] Marla Geha, Risa H. Wechsler, Yao-Yuan Mao, Erik J. Tollerud, Benjamin Weiner, Rebecca Bernstein, Ben Hoyle, Sebastian Marchi, Phil J. Marshall, Ricardo Muñoz, and Yu Lu. The saga survey. i. satellite galaxy populations around eight milky way analogs. *The Astrophysical Journal*, 847(1):4, 2017.

[66] Oliver Newton, Marius Cautun, Adrian Jenkins, Carlos S Frenk, and John C Helly. The total satellite population of the milky way. *Monthly Notices of the Royal Astronomical Society*, 479(3):2853–2870, May 2018.

[67] Takeshi Hirai. On the work of benjamin olinde rodrigues (1795-1851) – in particuler, on expression of spatial motions, 2020.

[68] Planck Collaboration, N. Aghanim, et al. Planck 2018 results. VI. Cosmological parameters. , 641:A6, September 2020.

[69] Facundo Rodriguez, Antonio D Montero-Dorta, Raul E Angulo, M Celeste Artale, and Manuel Merchán. The galaxy size–halo mass scaling relations and clustering properties of central and satellite galaxies. *Monthly Notices of the Royal Astronomical Society*, 505(3):3192–3205, May 2021.

[70] Ethan Ward et al. Evolution of the SizeMass Relation of Star-forming Galaxies Since z = 5.5 Revealed by CEERS. , 962(2):176, February 2024.

[71] Facundo Rodriguez, Antonio D. Montero-Dorta, Raul E. Angulo, M. Celeste Artale, and Manuel Merchán. The galaxy size-halo mass scaling relations and clustering properties of central and satellite galaxies. , 505(3):3192–3205, August 2021.

[72] Marcel S. Pawlowski and Pavel Kroupa. The Milky Way's disc of classical satellite galaxies in light of Gaia DR2. , 491(2):3042–3059, January 2020.

[73] Nassim Bozorgnia, Joseph Bramante, James M. Cline, David Curtin, David McKeen, David E. Morrissey, Adam Ritz, Simon Viel, Aaron C. Vincent, and Yue Zhang. Dark matter candidates and searches. *Canadian Journal of Physics*, 103(8):0128, September 2024.

[74] Tonatiuh Matos, F. Siddhartha Guzmán, and L. Arturo Ureña-López. Scalar field as dark matter in the universe. *Classical and Quantum Gravity*, 17(7):1707–1712, April 2000.

[75] Jordi Solís-López, Francisco S. Guzmán, Tonatiuh Matos, Victor H. Robles, and L. Arturo Ureña-López. Scalar field dark matter as an alternative explanation for the anisotropic distribution of satellite galaxies. *Physical Review D*, 103(8), April 2021.

Affirmation and Consent to the Checking of Plagiarism

I hereby confirm that I am the sole author of this thesis and have not used other sources and resources than the ones cited.

The thesis on hand is free of plagiarism. All information that has been extracted directly or indirectly from other works is marked as such and listed in the table of references.

This work has not been handed in as an assessed assignment with another examiner and has not been published before.

I have been informed that a plagiarism detection software will be used in order to check my thesis for its legitimacy. I am aware that my anonymized thesis will be analyzed in a secure domain of a server outside of the European Union and is temporarily saved there. For this, no personal data will be transmitted.

I hereby consent to the checking of my thesis through a plagiarism detection software under the aforementioned conditions.

Soumya Dhavale, 13. July, 2026